

**Beam-Energy Dependence of Directed Flow of Λ , $\bar{\Lambda}$, ϕ , K^\pm and K_s^0 in Au+Au
Collisions**

Current PAs:

**Yadav Pandit, Olga Evdokimov, Declan Keane, Prashanth Shanmuganathan,
Subhash Singha, Gang Wang and Nu Xu**

October 19, 2016

Contents

List of Figures	ii
List of Tables	ix
1 Analysis	1
1.1 Data	1
1.1.1 Event Selection	2
1.1.2 Centrality Selection	4
1.1.3 Track Selection	7
1.2 Particle Identification	8
1.2.1 π^\pm , K^\pm and $p(\bar{p})$ Identification	8
1.2.2 Reconstructing Λ , $\bar{\Lambda}$, K_S^0 and yields	11
1.2.2.1 Mixed Event Background Estimation	14
1.2.2.2 Side Band Background Estimation	16
1.2.2.3 Rotational Background Estimation	17
1.3 BBC Event Plane Calculation	17
1.3.0.1 Shift Correction	20
1.3.0.2 Event Plane Resolution	22
1.4 Directed Flow Measurements	24
1.4.1 Directed Flow of Charged Particles – π^\pm , K^\pm , $p(\bar{p})$	25

1.4.2	Directed Flow of Neutral Strange Particles – Λ , $\bar{\Lambda}$, K_S^0	25
1.4.3	Systematic Uncertainties	27
1.4.3.1	Detector Acceptance and Efficiency	28
2	Experimental Results	34
2.1	V_0 Invariant Mass Distributions	34
2.2	Rapidity Dependence of Directed Flow	38
2.2.1	Intermediate Centrality Au+Au Collisions	38
2.2.1.1	BES Data Analysis	39
2.2.1.2	UrQMD Model Calculations	43
2.2.1.3	Systematic Uncertainty Study	46
2.2.1.4	Net-Particle Directed Flow	52
2.2.1.5	Summary of Intermediate Centrality Results	54
2.2.2	Peripheral and Central Au+Au Collisions	56
2.2.3	Different Definitions of Wide Centrality Bins	59
2.3	Centrality Dependence of Directed Flow	61
Bibliography		81

List of Figures

1.1	Black data points shows normalized $\frac{dN_{\text{events}}}{dN_{\text{ch}}^{\text{raw}}}$ distributions for BES energies. The three shaded bands shows the centrality classes for central (0-10%) intermediate (10-40%) and peripheral (40-80%) collisions. The red histogram shows Monte Carlo Glauber simulations. This figure is reproduced from Ref. [81].	5
1.2	The plot on the left shows energy loss (dE/dx) for all particles as a function of electric charge times momentum in the TPC detector. The plot on the right shows dE/dx after particle identification cuts based on information from both TOF and TPC.	9
1.3	The mass ² distribution from the TOF detector without any cuts for particle identification.	11
1.4	V_0 decay topology diagram.	13
1.5	Illustration of mixed V_0 event background estimation for Λ at $\sqrt{s_{\text{NN}}} = 11.5$ GeV for 10-40% centrality. Panel (a) shows the signal+background and the mixed event background; panel (b) shows the same after the background is normalized; and panel (c) presents the invariant mass peak for Λ after background subtraction.	15
1.6	This plot illustrates the side band method in the case of the Λ signal. Vertical and horizontal axes are truncated for better clarity. S_0 , S_1 , and S_2 are signal + background entries, while B_0 , B_1 , and B_2 are background entries.	16

1.7	On the left is shown the west and east BBC detectors, for positive and negative η , respectively. On the right is shown the inner two rings of the BBC. The red numeral is tile number and blue numeral is the PMT number; these two are not always the same, since the read-out of tiles 7 and 9, and of 13 and 15, are coupled together.	18
1.8	Raw event plane distribution for east, west and full event plane calculations.	19
1.9	The shift-corrected event plane distribution for east, west and full event plane calculations. The distributions for 27 GeV and 39 GeV are scaled by factors of 0.75 and 0.5, respectively.	22
1.10	First order event plane resolution for all BES energies.	24
1.11	Histogram of signal+background (left) and normalized mixed-event background (right) for Λ as a function of invariant mass and $\phi - \Psi_{\text{RP}}$. These histograms are for 30-40% centrality Au+Au collisions at $\sqrt{s_{\text{NN}}} = 19.6$ GeV, with rapidity $0.2 < y \leq 0.4$	26
2.1	Invariant mass distribution of Λ for 10-40% centrality at $\sqrt{s_{\text{NN}}} = 11.5$ GeV. The solid blue histogram shows signal + background. The blue shaded area shows the mixed event background. The solid red area shows background-subtracted Λ candidates.	35
2.2	Invariant mass distribution of K_S^0 for 10-40% centrality at $\sqrt{s_{\text{NN}}} = 11.5$ GeV. The solid blue histogram shows signal + background. The blue shaded area shows the mixed event background. The solid red area shows background-subtracted K_S^0 candidates.	36
2.3	Λ invariant mass in thirty bins of $(\phi - \Psi_{\text{RP}})$ is shown for $-0.8 \leq y \leq -0.6$ and 30-40% centrality Au+Au collisions at a beam energy of 11.5 GeV.	37

2.4	K_S^0 invariant mass in thirty bins of $(\phi - \Psi_{RP})$ is shown for $0.4 \leq y \leq 0.6$ and 20-30% centrality Au+Au collisions at a beam energy of 7.7 GeV.	38
2.5	Directed flow (v_1) as a function of rapidity for p , Λ , \bar{p} , $\bar{\Lambda}$, K^\pm , K_s^0 and π^\pm for 10-40% centrality Au+Au collisions. Error bars are statistical. The v_1 magnitude is exceptionally large for $\bar{\Lambda}$ at 7.7 GeV, and therefore in that panel only, v_1 and its errors are divided by 5 to fit on the common vertical scale.	40
2.6	dv_1/dy near mid-rapidity as a function of beam energy for p , \bar{p} , π^\pm , Λ and $\bar{\Lambda}$ for 10-40% central Au+Au collisions. The dv_1/dy for $\bar{\Lambda}$ at 7.7 GeV is -0.13 ± 0.02 , which lies off-scale, below the lower end of the vertical axis. Error bars are statistical.	42
2.7	dv_1/dy near mid-rapidity as function of beam energy for K^+ , K^- and K_S^0 for 10-40% central Au+Au collisions. Error bars are statistical.	43
2.8	Directed flow as a function of rapidity for p , Λ , \bar{p} , $\bar{\Lambda}$, K^\pm , K_s^0 and π^\pm for 10-40% central UrQMD Au+Au collisions. Error bars are statistical. The v_1 magnitude is exceptionally large for \bar{p} and $\bar{\Lambda}$ at 7.7 and 11.5 GeV, and therefore for only for those four panels, v_1 and its errors are divided by 5 to fit on the common vertical scale.	44
2.9	The left panel shows dv_1/dy near mid-rapidity as function of beam energy for p , \bar{p} , π^\pm , Λ and $\bar{\Lambda}$ from UrQMD events for 10-40% central Au+Au collisions. Similarly, the right panel is for K^\pm and K_S^0 . Error bars are statistical.	45
2.10	Error from systematic variations is shown by the shaded band for v_1 vs. y , for particles Λ , $\bar{\Lambda}$ and K_S^0 , in 10-40% central collisions at a beam energy of 11.5 GeV.	47
2.11	Error from systematic variations is shown by the shaded band for v_1 vs. y , for particles Λ , $\bar{\Lambda}$ and K_S^0 , in 10-40% central collisions at a beam energy of 39 GeV.	48

2.12 Error from systematic variations is shown by the shaded band for v_1 vs. y , for particles p , \bar{p} , π^\pm and K^\pm , in 10-40% central collisions at a beam energy of 11.5 GeV. The systematic error for π^\pm is small and is not visible on the scale of this plot.	49
2.13 Error from systematic variations is shown by the shaded band for v_1 vs. y , for particles p , \bar{p} , π^\pm and K^\pm , in 10-40% central collisions at a beam energy of 39 GeV. The systematic error for π^\pm is small and is not visible on the scale of this plot.	50
2.14 The effect from different sources of systematic error is shown for dv_1/dy from 10-40% central collisions at a beam energy of 11.5 GeV on left and of 39 GeV on right. The cut number is defined in Table 1.4 and 1.5 for Λ and $\bar{\Lambda}$ baryons, and in Table 1.6 and 1.7 for K_S^0 . For Λ and $\bar{\Lambda}$, cut number 33 is the final data point with systematic and statistical errors, cut number 34 corresponds to systematic errors from event and track quality cuts, and cut number 35 includes only $V0$ systematic errors. For K_S^0 , cut number 19 is the final data point with systematic and statistical errors.	51
2.15 The effect from different sources of systematic error is shown for dv_1/dy from 10-40% central collisions at a beam energy of 11.5 GeV. The cut number is defined in Table 1.8 for p and \bar{p} , and in Table 1.9 for π^\pm and K^\pm . Cut number 15 is the final data point with systematic and statistical errors.	52
2.16 dv_1/dy near mid-rapidity at 10-40% centrality for net protons, net Λ s and net kaons.	54

2.17 Slope of v_1 near mid-rapidity as a function of beam energy for protons, antiprotons, Λ , $\bar{\Lambda}$, and π^\pm for 10-40% central collisions. Solid data points show BES data and shaded bands show UrQMD calculations. The dv_1/dy for $\bar{\Lambda}$ at 7.7 GeV is -0.13 ± 0.02 , which lies off-scale, below the lower end of the vertical axis. Error bars are statistical, while caps show systematic errors.	55
2.18 Slope of v_1 near mid-rapidity as a function of beam energy for K^\pm and K_s^0 for 10-40% central collisions. Solid data points show BES data and shaded bands show UrQMD calculations. Error bars are statistical, while caps show systematic errors.	56
2.19 Directed flow (v_1) as a function of rapidity for p , Λ , \bar{p} , $\bar{\Lambda}$, K^\pm , K_s^0 and π^\pm in 0-10% centrality Au+Au collisions. Error bars are statistical. The v_1 magnitude is exceptionally large for \bar{p} and $\bar{\Lambda}$ at 7.7 and 11.5 GeV, and hence for only those panels, v_1 and its errors are divided by 5 to fit on the common vertical scale.	57
2.20 Directed flow (v_1) as a function of rapidity for p , Λ , \bar{p} , $\bar{\Lambda}$, K^\pm , K_s^0 and π^\pm in 40-80% centrality Au+Au collisions. Error bars are statistical. The v_1 magnitude is exceptionally large for \bar{p} and $\bar{\Lambda}$ at 7.7 and 11.5 GeV, and hence for only those panels, v_1 and its errors are divided by 5 to fit on the common vertical scale.	58
2.21 Comparison of dv_1/dy for different combinations of centrality bins with the default intermediate-centrality class. Error bars are statistical.	60
2.22 dv_1/dy near midrapidity as a function of centrality for p . Top panel from STAR data and bottom panel is from UrQMD. Error bars are statistical. In general, systematic errors are comparable to statistical errors, but are omitted to reduce clutter.	62

2.23 dv_1/dy near midrapidity as a function of centrality for Λ . Top panel from STAR data and bottom panel is from UrQMD. Error bars are statistical. In general, systematic errors are comparable to statistical errors, but are omitted to reduce clutter.	63
2.24 dv_1/dy near midrapidity as a function of centrality for π^+ . Top panel from STAR data and bottom panel is from UrQMD. Error bars are statistical. In general, systematic errors are comparable to statistical errors, but are omitted to reduce clutter.	64
2.25 dv_1/dy near midrapidity as a function of centrality for π^- . Top panel from STAR data and bottom panel is from UrQMD. Error bars are statistical. In general, systematic errors are comparable to statistical errors, but are omitted to reduce clutter.	65
2.26 dv_1/dy near midrapidity as a function of centrality for K^+ . Top panel from STAR data and bottom panel is from UrQMD. Error bars are statistical. In general, systematic errors are comparable to statistical errors, but are omitted to reduce clutter.	66
2.27 dv_1/dy near midrapidity as a function of centrality for K^- . Top panel from STAR data and bottom panel is from UrQMD. Error bars are statistical. In general, systematic errors are comparable to statistical errors, but are omitted to reduce clutter.	67
2.28 dv_1/dy near midrapidity as a function of centrality for K_S^0 . Top panel from STAR data and bottom panel is from UrQMD. Error bars are statistical. In general, systematic errors are comparable to statistical errors, but are omitted to reduce clutter.	68

2.29 Systematic error for dv_1/dy as a function of centrality is shown for p , Λ , π^+ and π^- at a beam energy of 11.5 GeV.	70
2.30 Systematic error for dv_1/dy as a function of centrality is shown for p , Λ , π^+ and π^- at a beam energy of 39 GeV.	71
2.31 Systematic error for dv_1/dy as a function of centrality is shown for K^\pm and K_S^0 at a beam energy of 39 GeV.	72
2.32 Systematic error for dv_1/dy as a function of centrality is shown for K^\pm and K_S^0 at a beam energy of 39 GeV.	73

List of Tables

1.1	Statistics and energy-dependent cuts and parameters.	3
1.2	$N_{\text{ch}}^{\text{raw}}$ for nine centrality bins at BES energies.	7
1.3	V0 topological cuts for Λ and K_S^0 particles. A momentum-dependent lower mass cut for pions is selected to reject contamination from electron misidentification. All lengths are in centimeters and all masses are in GeV/c^2	14
1.4	Minimum and maximum event and track cuts used for systematic study of $\Lambda(\bar{\Lambda})$. The cut number is a unique identifier assigned to each minimum and maximum cut value, used later to identify that variation in the plots. All lengths are in centimeters, all momenta are in GeV/c and all masses are in GeV/c^2	30
1.5	Minimum and maximum p_T , V0 and decay daughter track cuts used to estimate systematic errors for $\Lambda(\bar{\Lambda})$. The cut number is a unique identifier assigned to each minimum and maximum cut, used later to identify that variation in the plots. All lengths are in centimeters, all momenta are in GeV/c and all masses are in GeV/c^2	31
1.6	Minimum and maximum event and track cuts used to estimate systematic errors for K_S^0 . The cut number is a unique identifier assigned to each minimum and maximum cut, used later to identify that variation in the plots. All lengths are in centimeters.	31

1.7	Minimum and maximum p_T , $V0$ and decay daughter track cuts used to estimate systematic errors for K_S^0 . The cut number is a unique identifier assigned to each minimum and maximum cut, used later to identify that variation in the plots. All lengths are in centimeters, and all momenta are in GeV/c .	32
1.8	Minimum and maximum event and track cuts used to estimate systematic errors for protons. The cut number is a unique identifier assigned to each minimum and maximum cut, used later to identify that variation in the plots. All lengths are in centimeters, all momenta are in GeV/c and all masses are in GeV/c^2	33
1.9	Minimum and maximum events cuts used to estimate systematic errors for pions and kaons. The cut number is a unique identifier assigned to each minimum and maximum cut, used later to identify that variation in the plots. All lengths are in centimeters, all momenta are in GeV/c and all masses are in GeV/c^2	33
2.1	Summary of the event statistics used in UrQMD simulations. For reference, real event statistics are also shown.	45
2.2	Alternative groupings of coarse centrality bins.	60

Chapter 1

Analysis

This chapter describes the analysis techniques used in this dissertation. The first part of this chapter describes the quality assurance selections (cuts) imposed on the available data. Second, centrality selection and event plane estimation are discussed. Third, particle identification techniques are discussed. Finally, I explain the directed flow calculation methods and conclude with systematic uncertainty estimation.

1.1 Data

During the Beam Energy Scan program, the STAR experiment successfully recorded data from Au+Au collisions for center of mass energies ($\sqrt{s_{NN}}$) 7.7, 11.5, 14.5, 19.6, 27 and 39 GeV. The data consist of information about each gold on gold collision (event) and associated trigger information, and about the signals recorded in various detector sub-systems. These data are pre-processed using generic software which identifies the tracks and hence the momentum vectors of the produced particles in each event, and stores this higher level information in so-called microDST files for physics analysis.

1.1.1 Event Selection

When RHIC and its experiments (STAR and PHENIX) are fully functional, data are recorded continuously for typically around twenty weeks per year. During data-taking, events are recorded in files, where each file corresponds to one 'run'. A run can last for as little as a second or two, or as long as many tens of minutes. Due to the extended period of some runs, the conditions of the beam or the detector setup may deteriorate. For example, a poorly focused beam can cause high background rates, or an important part of a detector might stop working. Runs from such periods are normally flagged and removed. The mean interaction rates, the mean transverse momentum, the mean vertex position, and the mean multiplicity of events are among the quantities monitored closely for the purpose of quality assurance.

After removing bad runs, the good events in each retained run are selected for the analysis using a so-called "minimum-bias" trigger, where minimum bias means that an effort is made to accept all centralities (i.e., all impact parameters), up to and including peripheral collisions. A minimum-bias trigger at BES energies requires a coincidence between the east and west Zero Degree Calorimeters (ZDC), and/or between the east and west Vertex Position Detectors (VPD), and/or between the east and west Beam Beam Counters (BBC). Due to the large beam emittance, especially at lower beam energy, Au ions may sometimes collide with the beam pipe (2.00 cm inner radius at 14.5 GeV and 3.81 cm inner radius at all other beam energies) rather than with another Au ion. To eliminate these events, we require the primary vertex of events to lie within 1 cm from the beam axis at 14.5 GeV, and within 2 cm at the other beam energies. At 14.5 GeV, the beam axis was offset from the center of the beam pipe according to $(x, y) = (0, -0.89)$ cm. The z -position of the vertex was optimized during the data taking using the online High Level Trigger (HLT). Then, from offline studies, z -vertex cuts are applied to ensure the quality of events. This z -vertex cut

also ensures that the acceptance for tracks in an event between the east and west sides of detectors is consistent.

The term pileup refers to an event where particles from more than one single collision are recorded in that event. This can happen, for example, if luminosity is high and trigger criteria are loose. Since some tracks belong to a non-triggered event, these tracks do not have valid TOF information. Requiring each event to have at least 5 TOF hits can eliminate these events. In addition, we also require the reconstructed charged particle multiplicity in each events to be greater than 5, and we allow at most 5 primary vertices in an event. To further remove background events, we require 15 or more summed ADC counts in each of the east and west BBC detectors for 7.7, 11.5 and 19.6 GeV, and at least 75 counts for 14.5, 27, and 39 GeV. After applying these event quality cuts, the available good events for further analysis are summarized in Table 1.1 along with the other beam-energy-dependent cuts and parameters.

$\sqrt{s_{\text{NN}}}$ (GeV)	Events (10^6)	Minimum-biase Trigger ID	$ V_z $ (cm)	BBC ADC sum
7.7	4	290001, 290004	70	15
11.5	12	310004, 310014	50	15
14.5	20	440005, 440015	50	75
19.6	36	34000, 340011, 340021	50	15
27	70	360001, 360002	50	75
39	130	280001, 280002	40	75

Table 1.1: Statistics and energy-dependent cuts and parameters.

1.1.2 Centrality Selection

The degree of overlap between the two nuclei in a nucleus-nucleus collision is called centrality, and it is an experimental proxy for the impact parameter (b). Impact parameter, which cannot be measured experimentally, is the distance between the two colliding nuclei at their closest point, assuming the nuclei follow straight-line trajectories. If the two nuclei are fully overlapped ($b = 0$, a head-on collision), this is called a central collision. This type of collision is expected to produce a hotter and denser medium than a peripheral collision, where nuclei only partly overlap. In a central collision, a large particle multiplicity is expected and a larger fraction of the available energy is deposited in the transverse direction. The nucleons in the overlapping region are called participants and these nucleons interact through inelastic collisions. Since the properties of the medium formed after the collision depends not only on the energy of the initial nucleons, but also depends on the centrality, we study the available data in bins of centrality.

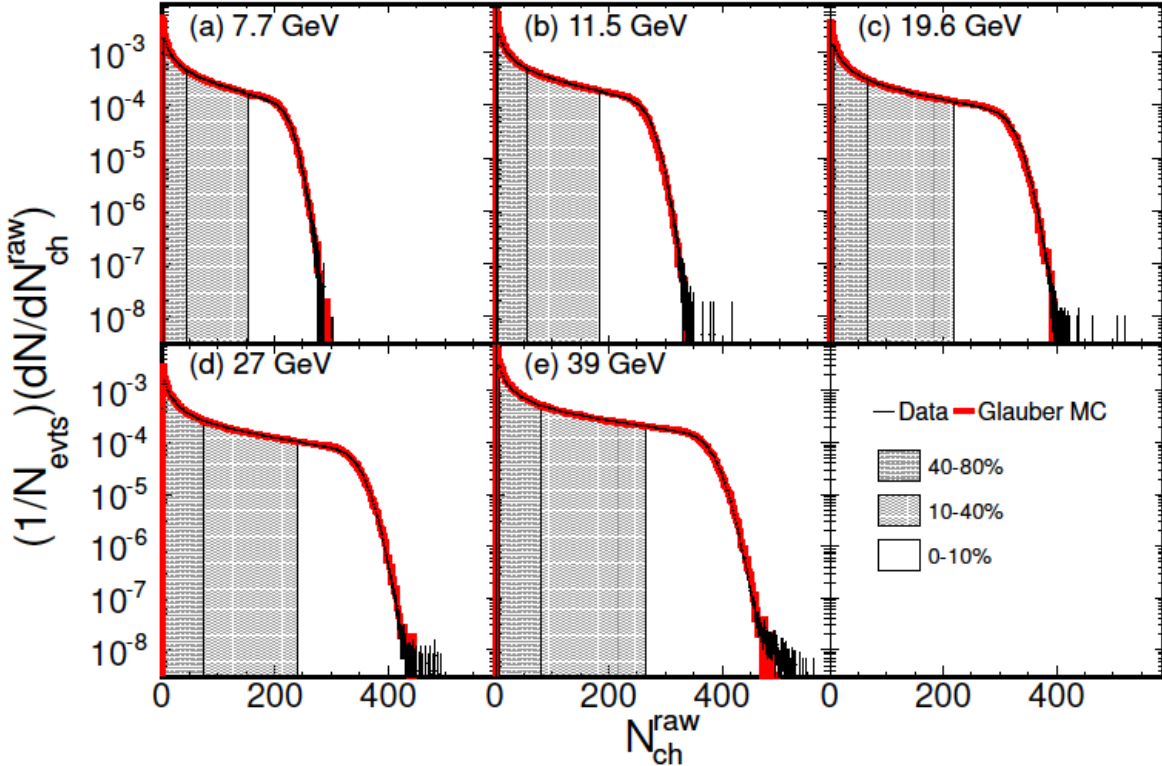


Figure 1.1: Black data points shows normalized $\frac{dN_{\text{events}}}{dN_{\text{ch}}^{\text{raw}}}$ distributions for BES energies. The three shaded bands shows the centrality classes for central (0-10%) intermediate (10-40%) and peripheral (40-80%) collisions. The red histogram shows Monte Carlo Glauber simulations. This figure is reproduced from Ref. [81].

The collision centrality is calculated based on uncorrected charged particle multiplicity distributions, $\frac{dN_{\text{events}}}{dN_{\text{ch}}^{\text{raw}}}$. Reconstructed charged particle multiplicity, $N_{\text{ch}}^{\text{raw}}$ (known as reference multiplicity) is calculated in the TPC for $|\eta| < 0.5$ and track DCA less than 3 cm. The former selection ensures uniform acceptance regardless of the primary vertex position along the z direction, while the latter largely eliminates tracks from weak decay vertices. Another noteworthy factor in relation to $N_{\text{ch}}^{\text{raw}}$ is the TPC reconstruction efficiency. Especially during BES data taking, there were periods when at least one of the TPC sectors was not working, which requires a correction to the reconstructed charged multiplicity (known as corrected

reference multiplicity). Since a dead sector only affects one side of the TPC at a time, the reconstructed track efficiency varies with the z -coordinate of a collision vertex. The TPC efficiency is calculated from the data as a function of the z -coordinate, and raw multiplicity is weighted accordingly. The observed charged particle multiplicity distribution is well described by Glauber Monte Carlo (MC) simulations. Figure 1.1 shows $N_{\text{ch}}^{\text{raw}}$ distributions for BES data and the associated results from Glauber MC simulations with a two-component model [82] fit to the simulated multiplicity distribution.

The biggest disagreement in multiplicity simulations arises due the trigger inefficiency for very peripheral events. Such events have very few tracks and do not provide a reliable event vertex. These inefficiencies are corrected by weighting particle yields by the ratio of simulations to data. Glauber MC calculations and details of fitting the multiplicity distributions are explained in reference [83]. When a MC Glauber fit is available, collision centrality can be determined from the fit to the Cumulative Distribution Function (CDF) for a given reference multiplicity. Table 1.2 shows the reference multiplicity values for BES data in nine centrality bins for the narrowest bin size used in this analysis.

Centrality	BES energies($\sqrt{s_{NN}}$) GeV					
	percentile	7.7	11.5	14.5	19.6	27
5%	185	221	239	263	288	326
10%	154	184	200	220	241	285
20%	106	127	138	152	168	199
30%	72	86	93	102	114	135
40%	46	56	59	66	74	88
50%	28	34	36	40	45	54
60%	16	19	20	23	26	30
70%	8	10	11	12	13	16
80%	4	5	5	6	6	7

Table 1.2: $N_{\text{ch}}^{\text{raw}}$ for nine centrality bins at BES energies.

1.1.3 Track Selection

Several cuts are applied to reconstructed charged particle tracks to ensure data quality. In this section, I explain each cut in detail. First, to eliminate false tracks formed by hits belonging to many different particles, the number of fit points in the TPC is required to be greater than 15. Then to avoid track splitting (where one long track is reconstructed as two shorter tracks), we require $\frac{\text{number of TPC fit points}}{\text{maximum number of possible fit points}} \geq 0.52$. Pileup tracks are identified during data production and flagged with an ID greater than 1000. I require all tracks to have $0 < \text{flag} < 1000$. These are the basic track quality cuts used during track selection; I discuss track selection criteria for particle identification and V0 reconstruction in the following sections.

1.2 Particle Identification

1.2.1 π^\pm , K^\pm and $p(\bar{p})$ Identification

Long-lived charged particles are identified using both energy loss information from the TPC and time of flight information from the TOF barrel. Some particles are identified using the ionization energy loss, dE/dx , in the gas of the TPC. The left panel of Figure 1.2 shows an example. For a minimum ionizing particle (MIP) that produces a single track with the maximum possible number of TPC pad rows crossed (45), the dE/dx resolution is found to be about 6 to 8% [75]. At lower momenta ($0.3 \leq p_T \leq 0.6$ GeV/ c), the energy loss bands show clear separation between particle types. The energy loss bands decrease with increasing momentum, reaches a minimum near $\beta\gamma \sim 3$ for every particle type, and then increase again due to relativistic rise. For the STAR TPC, the Bichsel function [84] is a good approximation for predicting the center of dE/dx bands. The normalized energy loss can be written [85]

$$n\sigma_{\text{particle}} = \ln \left(\frac{dE/dx_{\text{particle}}}{\langle dE/dx \rangle_{\text{Bichsel}}} \right) / \sigma_{\text{particle}} \quad (1.1)$$

where σ_{particle} is the TPC dE/dx resolution. The criterion $|n\sigma| \leq 2$ along with the other PID cuts gives a reasonably good separation between pions, kaons and protons.

Particle identification based on dE/dx in the TPC is further refined using TOF hit information. The squared mass (m^2) of the track is calculated from the time of flight and momentum information from the TPC:

$$\text{TOF mass}_{\text{track}}^2 = p_{\text{tot}}^2 \left(\frac{1}{\beta^2} - 1 \right) \quad (1.2)$$

where p_{tot} is the particle's total momentum, $\beta = l/(ct_{\text{TOF}})$, and in turn, l is the particle's path length, c is the speed of light, and t_{TOF} is the time of flight.

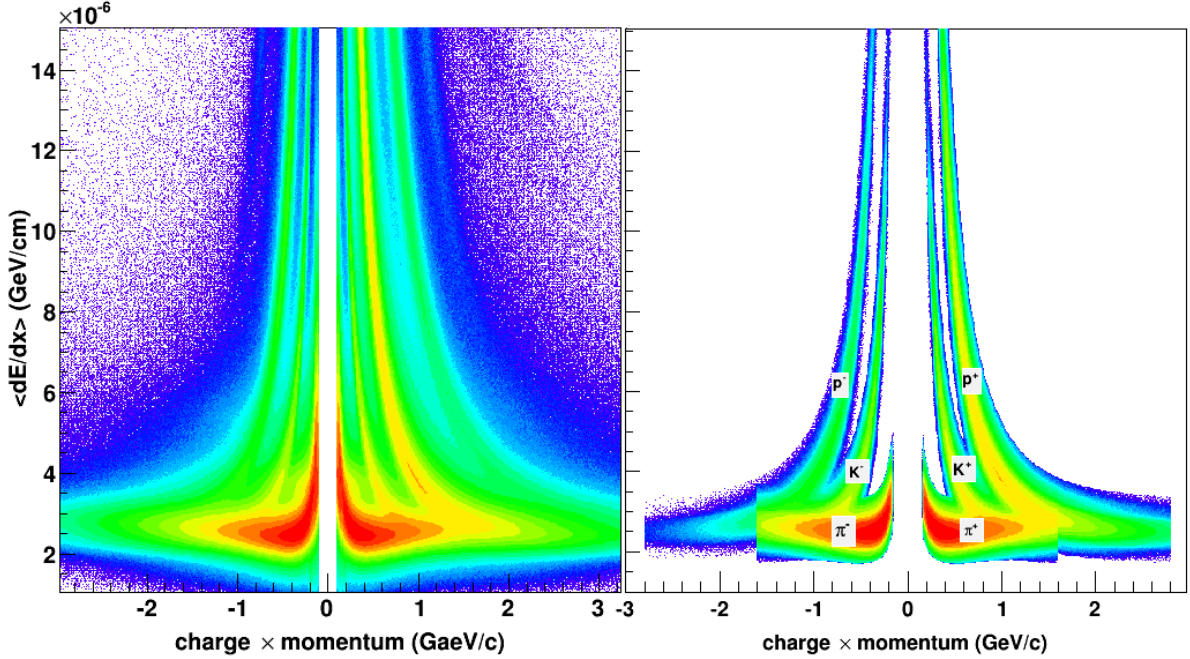


Figure 1.2: The plot on the left shows energy loss (dE/dx) for all particles as a function of electric charge times momentum in the TPC detector. The plot on the right shows dE/dx after particle identification cuts based on information from both TOF and TPC.

Without any particle identification cuts, the squared mass distribution for charged particles is shown in Figure 1.3. We select π^\pm , K^\pm and $p(\bar{p})$ based on the following m^2 selections:

$$\pi^\pm : -0.01 < m^2 < 0.10 \text{ GeV}^2/\text{c}^4$$

$$K^\pm : 0.20 < m^2 < 0.35 \text{ GeV}^2/\text{c}^4$$

$$p(\bar{p}) : 0.8 < m^2 < 1.0 \text{ GeV}^2/\text{c}^4$$

A small negative value for pions m^2 chosen to avoid cutting on the $n\sigma$ band. To further improve the purity of particle identification, the following cuts were also imposed on p_T and p_{tot} :

$$\pi^\pm : 0.2 \text{ GeV/c} \leq p_T \text{ and } p_{\text{tot}} \leq 1.6 \text{ GeV/c}$$

$$K^\pm : 0.2 \text{ GeV/c} \leq p_T \text{ and } p_{\text{tot}} \leq 1.6 \text{ GeV/c}$$

$$p(\bar{p}) : 0.4 \text{ GeV/c} \leq p_T \leq 2.0 \text{ GeV/c} \text{ and } p_{\text{tot}} \leq 2.8 \text{ GeV/c}$$

In addition, to exclude tracks from secondary vertices, we require a distance of closest approach to the primary vertex (DCA) of 3 cm or less. After imposing all of the above charged particle identification cuts, the resulting dE/dx distribution is shown in the right panel of Figure 1.2. To maintain consistency across published results, this study uses the same cuts for protons and pions as in a published STAR paper on directed flow for protons and pions [49].

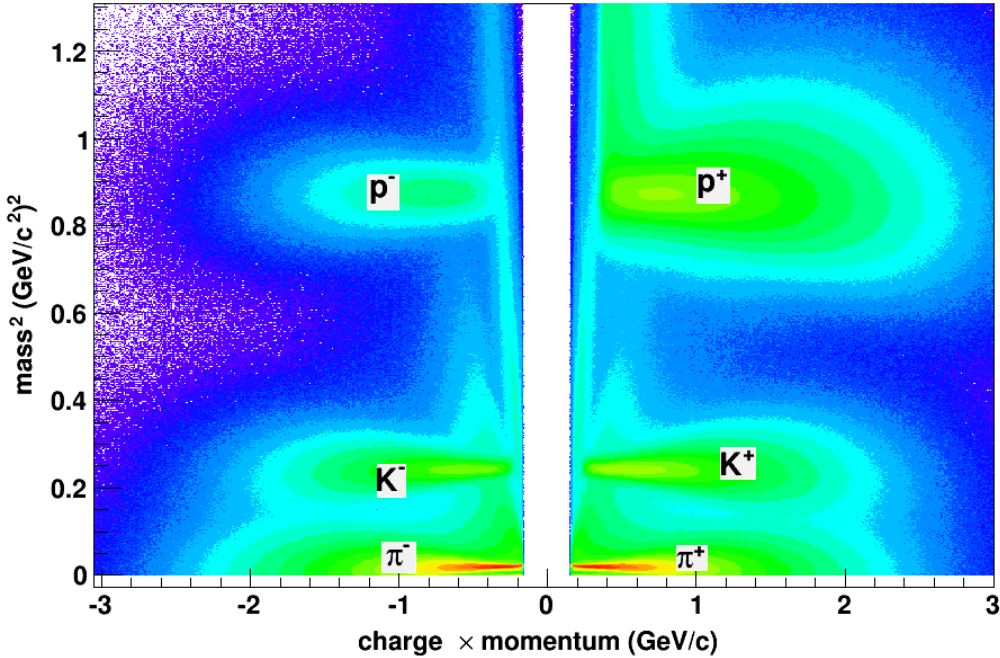


Figure 1.3: The mass² distribution from the TOF detector without any cuts for particle identification.

1.2.2 Reconstructing Λ , $\bar{\Lambda}$, K_S^0 and yields

The secondary vertices in a nuclear collision can be categorized into three groups:

- Kink vertices: a charged particle decays into a charged and neutral daughter.
- $V0$ vertices: a neutral particle decays into two charged daughters.
- Cascade vertices: a charged particle decays into a charged plus neutral daughter, and then the neutral particle decays into two charged particles.

In this dissertation, I am interested in the weakly-decaying neutral strange particles Λ , $\bar{\Lambda}$ and K_S^0 , all of which can be detected via their $V0$ topology (two oppositely charged daughters at a secondary vertex) as follows [86, 87]:

- Λ (1115.68 MeV/c²) $\longrightarrow p^+$ (939.56 MeV/c²) + π^- (139.57 MeV/c²) (63% branching fraction)
- $\bar{\Lambda}$ (1115.68 MeV/c²) $\longrightarrow p^-$ (939.56 MeV/c²) + π^+ (139.57 MeV/c²) (63% branching fraction)
- K_S^0 (497.614 MeV) $\longrightarrow \pi^+$ (139.57 MeV/c²) + π^- (139.57 MeV/c²) (69% branching fraction)

Figure 1.4 shows a topological map of a $V0$ decay. Here the tracks P^+ and P^- are positive and negative charged decay daughters, respectively, PV denotes the primary vertex, and DCA denotes distance of closest approach. The coordinates of the positive and negative tracks are combined at the mid-point of the DCA between the two daughter tracks (DCA P^+ to P^- in the diagram) to form the parent particle decay vertex. The 4-momentum and other kinematic variables of the parent particle is obtained from the daughter momentum vectors at this same DCA [88]. If the reconstructed decay vertex passes the selection criteria (discussed in the next section), then the invariant mass of the parent particle is calculated using the mass hypothesis

$$m = \sqrt{\left(\sqrt{m_+^2 + P_+^2} + \sqrt{m_-^2 + P_-^2}\right)^2 - (P_+^2 + P_-^2)} \quad (1.3)$$

where m_+ and m_- are the appropriate daughter particle masses, as listed above.

There is a combinatoric background arising from unrelated pairs of particles from the primary vertex accidentally having an invariant mass near that of the relevant particle. This combinatoric background was reduced by directly identifying the decay daughters from dE/dx and/or m^2 information using the TPC and/or TOF. Since only 65% of the tracks have valid TOF information, m^2 cuts are not applied at all $V0$ vertices. A $|n\sigma| \leq 3$ cut is applied

to normalized dE/dx for all particles, while an m^2 cut is applied to tracks which have TOF hit information. To compensate for the missing TOF information, tighter topological cuts are applied to tracks which have only TPC information. Several topological cuts are chosen from the helix parameters of reconstructed TPC tracks, such as DCA between daughter tracks, DCA to daughter tracks from primary vertex, DCA between the V_0 vertex and the primary vertex, and the decay length of the V_0 particle. These cuts are used in all STAR V_0 analyses and are optimized for maximum significance by systematically varying the cuts [27]. The selection criteria for V_0 vertices are summarized in table 1.3.

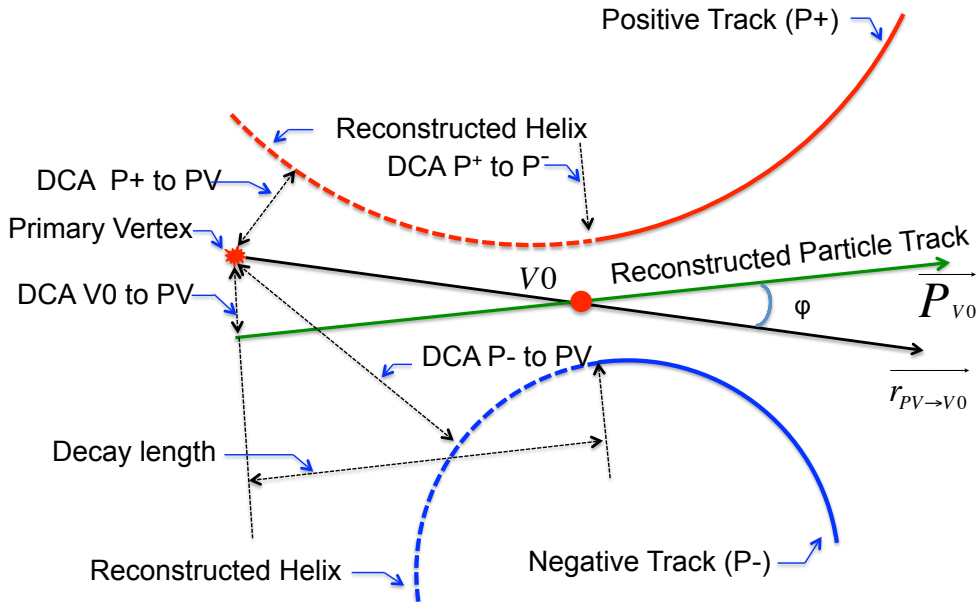


Figure 1.4: V_0 decay topology diagram.

V0 cuts	$\Lambda(\bar{\Lambda})$					K_S^0
	Protons & pions have TOF	Only Protons have TOF	Only Pions have TOF	Neither have TOF	Independent of TOF	
$n\sigma_{\text{Pion}}$	$< 3.0 $					
$n\sigma_{\text{Proton}}$	$< 3.0 $					-
TOF mass ² Proton	$0.5 < m^2 < 1.5$					-
TOF mass ² Pion	$(0.017 - 0.013 \times p_{\text{tot}}) < \text{mass}^2 < 0.04$					
DCA daughters	< 1.00					
DCA Protons to PV	>0.1	>0.15	>0.5	>0.6	-	
DCA Pion to PV	>0.7	>0.8	>1.5	>1.7	>0.7	
DCA V ₀ to PV	>1.3	>1.2	>0.75	>0.75	>0.8	
Decay lenght	>2.0	>2.5	>3.5	>4.0	>3.0	

Table 1.3: V0 topological cuts for Λ and K_S^0 particles. A momentum-dependent lower mass cut for pions is selected to reject contamination from electron misidentification. All lengths are in centimeters and all masses are in GeV/c^2 .

1.2.2.1 Mixed Event Background Estimation

The combinatoric background from uncorrelated particles is removed using the mixed-event technique. A temporary buffer of events is constructed using only the event and track parameters needed to form V0 vertices. Mixed events are chosen to have the same global properties as real events, which in the present case means centrality, vertex position along the z -axis (V_z) and event plane azimuth (Ψ_{RP}). Available events are divided into nine bins of centrality, ten bins for V_z and 30 bins for Ψ_{RP} , which makes a total of 2700 event classes. For each event class, five mixed events are built on the fly for each BES energy, except for 7.7 GeV. Because of the limited number of good positive and negative tracks in a mixed event class for the later case, 15 mixed events are built to increase the probability of a V0 vertex being reconstructed. After the required number of mixed events for a particular event class is acquired and V0 vertices are reconstructed, the corresponding event buffer class is deleted.

When a particular buffer of an event class is filled, each positive track in a selected event is combined with each negative track in the remaining events to reconstruct the $V0$ vertex. The above procedure for choosing positive tracks in a event is repeated for the remaining events in the buffer. Event mixing always results in a large number of reconstructed mixed events, and thus results in a larger number of reconstructed $V0$ background candidates than in the real event sample. Therefore, the mixed event background is normalized away from the mass region of the peak. The normalization region is chosen for Λ ($\bar{\Lambda}$) on the high-mass side of the peak, and for K_S^0 , both sides of the mass peak are used. This procedure is illustrated in Figure 1.5 for Λ . Panel (a) shows the reconstructed Λ candidates (signal + background) as a red histogram, and the mixed event background is the grey shaded area. In panel (b), the mixed event background is normalized, and in panel (c), the normalized background has been subtracted from the $V0$ candidates.

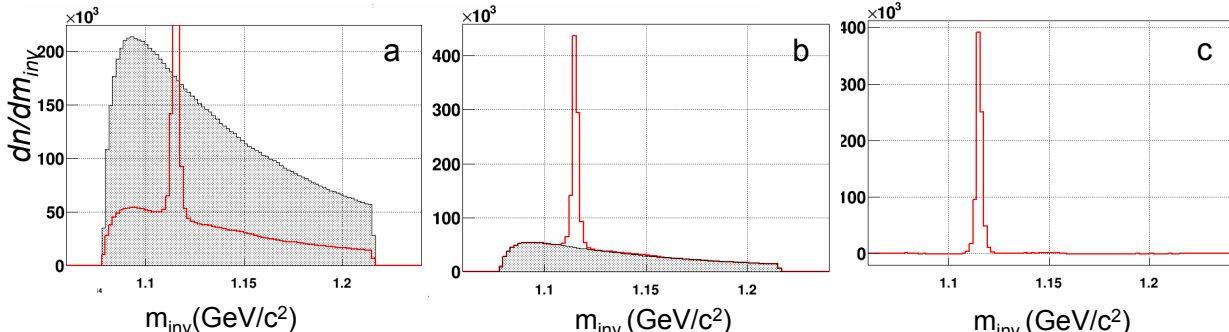


Figure 1.5: Illustration of mixed $V0$ event background estimation for Λ at $\sqrt{s_{NN}} = 11.5 \text{ GeV}$ for 10-40% centrality. Panel (a) shows the signal+background and the mixed event background; panel (b) shows the same after the background is normalized; and panel (c) presents the invariant mass peak for Λ after background subtraction.

1.2.2.2 Side Band Background Estimation

In addition to the mixed-event method, a side band method is also used to crosscheck the results. Figure 1.6 shows results of this method, where the background is estimated from an average of the signal+background in a region just below and just above the observed peak in the signal+background. Here we assume that the background linearity is good. Regions B_1 and B_2 are chosen each to be half the width of region B_0 . So B_0 can be approximated as $(B_1 + B_2)$. Further, we assume $S_1 \approx B_1$ and $S_2 \approx B_2$. Then the corrected yield is $S_0 - (S_1 + S_2)$. The results show excellent agreement between the mixed-event method and the side band method.

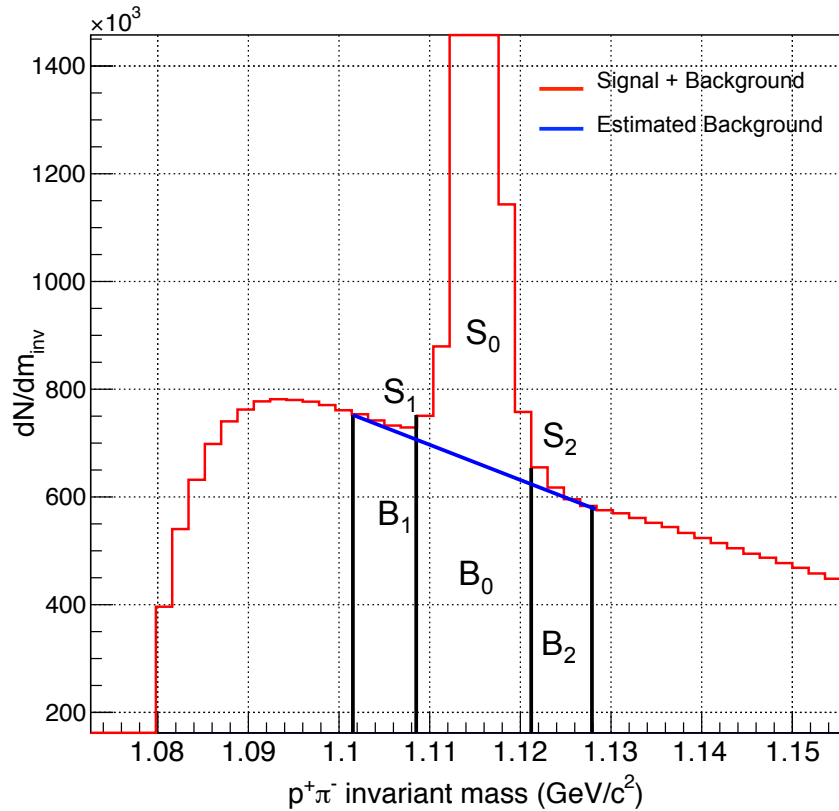


Figure 1.6: This plot illustrates the side band method in the case of the Λ signal. Vertical and horizontal axes are truncated for better clarity. S_0 , S_1 , and S_2 are signal + background entries, while B_0 , B_1 , and B_2 are background entries.

1.2.2.3 Rotational Background Estimation

This method is used for background estimation in many heavy-ion studies, and was the first method explored when I started this dissertation analysis. But this method can have a serious bias when used for $V0$ flow [89]. In the rotational background method, one of the daughter tracks (protons, in my tests) is rotated by 180° in the transverse plane, and the resulting tracks are used to reconstruct the $V0$ background. Rotation of protons causes the background v_1 to have the opposite sign from the signal v_1 , since the daughter proton carries most of the momentum of the parent Λ . This highly undesirable back-to-back correlation between signal and background is clearly seen when the rotational background method is investigated.

1.3 BBC Event Plane Calculation

The plane formed by the beam axis and the impact parameter is known as the reaction plane. Experimentally, it impossible to find the true reaction plane in any given collision [37], so we approximate it with the observed event plane calculated from the anisotropy of produced particles. At $\sqrt{s_{NN}}$ up to 39 GeV, the BBC detectors offer a reasonably good event plane resolution. The inner two rings of the east and west BBC are used to calculate the event plane. The BBC and TPC + TOF are separated by a large η gap. This η gap ensures there is minimal non-flow contribution to the flow calculations in $|\eta| \leq 1.0$. The n^{th} harmonic event plane vector, \vec{Q}_n , is defined by the equations

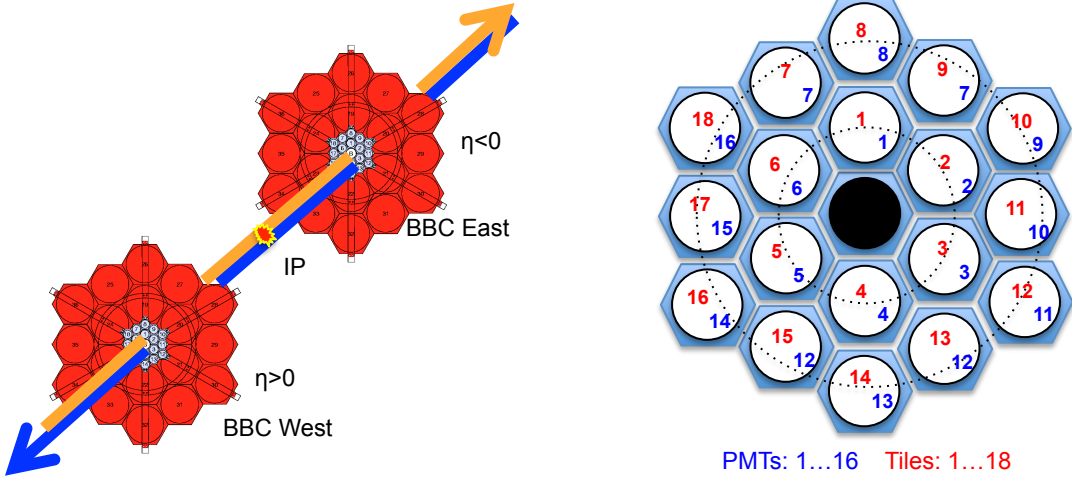


Figure 1.7: On the left is shown the west and east BBC detectors, for positive and negative η , respectively. On the right is shown the inner two rings of the BBC. The red numeral is tile number and blue numeral is the PMT number; these two are not always the same, since the read-out of tiles 7 and 9, and of 13 and 15, are coupled together.

$$Q_{n,x} = \sum_i w_i \cos(n\phi_i) = Q_n \cos(n\Psi_n) \quad (1.4)$$

$$Q_{n,y} = \sum_i w_i \sin(n\phi_i) = Q_n \sin(n\Psi_n) \quad (1.5)$$

$$w_i = \frac{A_i}{\sum A_i} \quad (1.6)$$

Here, ϕ_i is the azimuth of the center of the i^{th} tile of the BBC, and w_i the normalized and gain-corrected ADC value (the equivalent of energy deposition) in the i^{th} tile. The normalization for the east and west sides of the BBC is set independently.

The event plane angle Ψ_n for the n^{th} harmonic is calculated using

$$\Psi_n = \frac{\tan^{-1}(Q_{n,y}/Q_{n,x})}{n} \quad (1.7)$$

The imperfect azimuthal symmetry of the TPC (affected by imperfections such as sector boundaries, non-uniform efficiency, temporarily dead channels, etc.) makes the reconstructed event plane distribution non-uniform (not-flat), and could bias flow measurements if not corrected [90]. Figure 1.8 shows a 1st-order raw event plane distribution for BES energies. To correct this non-uniformity, three methods are widely used, namely phi weighting, recentering, and shifting. In this dissertation, the shifting method is used.

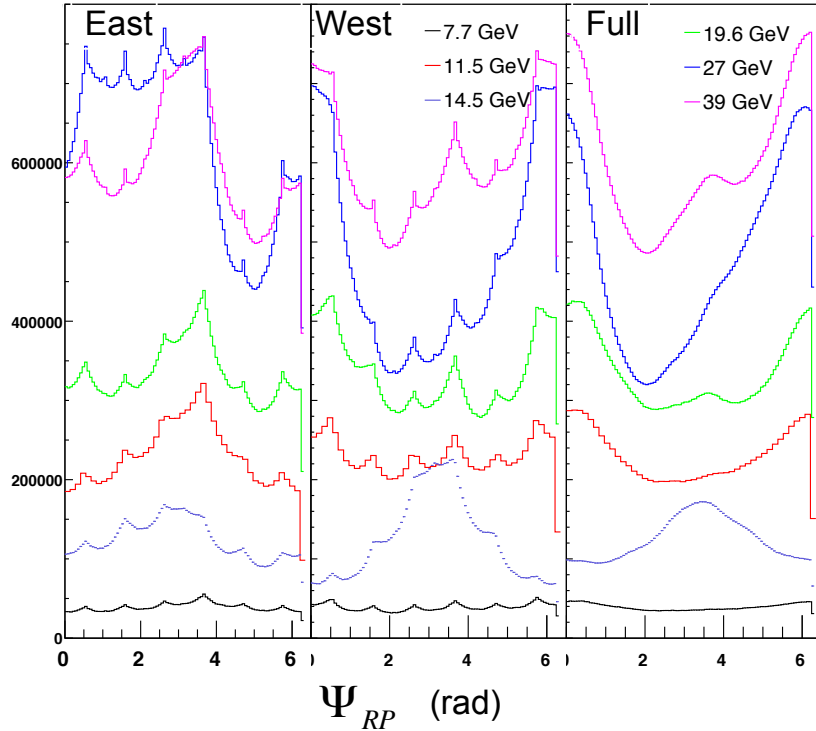


Figure 1.8: Raw event plane distribution for east, west and full event plane calculations.

1.3.0.1 Shift Correction

In the shift correction method [91], a correction term is chosen to force the n^{th} Fourier harmonic in the raw event plane distribution, Ψ , to become flat. The raw event plane distribution can be expanded in a Fourier series as follows:

$$\frac{dN}{d\Psi} = \frac{a_0}{2} + \sum_n (a_n \cos n\Psi + b_n \sin n\Psi) \quad (1.8)$$

where coefficients a_n and b_n are

$$a_n = \frac{1}{\pi} \int_{-\pi}^{\pi} \frac{dN}{d\Psi} \cos n\Psi d\Psi, \quad n = 0, 1, 2, \dots \quad (1.9)$$

$$b_n = \frac{1}{\pi} \int_{-\pi}^{\pi} \frac{dN}{d\Psi} \sin n\Psi d\Psi, \quad n = 0, 1, 2, \dots \quad (1.10)$$

Then the corrected event plane Ψ' can be written

$$\Psi' = \Psi + \Delta\Psi \quad (1.11)$$

where $\Delta\Psi$ is the correction term and can be written in the form

$$\Delta\Psi = \sum_n (A_n \cos n\Psi + B_n \sin n\Psi) \quad (1.12)$$

By imposing the condition of a flat distribution on Eq. 1.11 (requiring the n^{th} Fourier harmonic to vanish), it is found that

$$\frac{dN}{d\Psi'} = \frac{N}{2\pi} = \frac{a_0}{2} \quad (1.13)$$

Now we can re-arrange Eq. 1.8

$$\frac{dN}{d\Psi} = \frac{dN}{d\Psi'} \frac{d\Psi'}{d\Psi} = \frac{a_0}{2} \left[1 + \sum (-nA_n \sin n\Psi + nB_n \cos n\Psi) \right] \quad (1.14)$$

Comparing the above with Eq. 1.8, we find the coefficients A_n and B_n and the new corrected event plane distribution:

$$\Psi' = \Psi + \sum \frac{1}{n} (-\langle \sin 2n\Psi \rangle \cos 2n\Psi + \langle \cos 2n\Psi \rangle \sin 2n\Psi) \quad (1.15)$$

Here, the angle brackets mean the average over a large number of events. To get a reasonably flat event plane distribution, it is necessary to repeat the calculation of the correction term multiple times, first to initialize the parameters, and then to find the correction terms. Also, in this analysis, we use up to the 20th harmonic to flatten the raw distribution. Figure 1.9 shows such a shift-corrected 1st-order event plane distribution for BES energies.

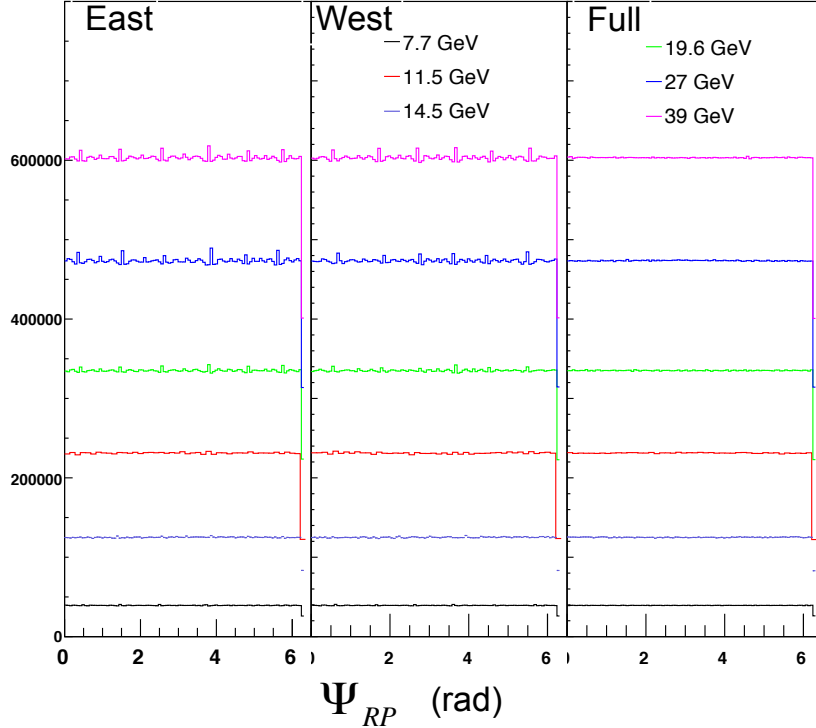


Figure 1.9: The shift-corrected event plane distribution for east, west and full event plane calculations. The distributions for 27 GeV and 39 GeV are scaled by factors of 0.75 and 0.5, respectively.

1.3.0.2 Event Plane Resolution

The event plane resolution depends on several factors, including the multiplicity of the particles used in the determination of the event plane. The event plane resolution for each harmonic is given by [37]

$$R_n = \langle \cos n(\Psi_n - \Psi_{RP}) \rangle \quad (1.16)$$

Here, angle brackets mean the average over large number of events. The resolution of the event plane strongly depends on centrality, so these corrections should be applied in small

centrality bins (in our analysis, 10% centrality increments). East and west BBC detectors are independent; therefore the correlation between two event planes can be written

$$\langle \cos n (\Psi_{\text{east}} - \Psi_{\text{west}}) \rangle = \langle \cos n (\Psi_{\text{east}} - \Psi_{\text{RP}}) \rangle \langle \cos n (\Psi_{\text{west}} - \Psi_{\text{RP}}) \rangle \quad (1.17)$$

If we assume that the two sub-detectors (east and west) have similar event plane resolution, then the sub-event plane resolution can be written

$$R_{n,\text{sub}} = \sqrt{\langle \cos n (\Psi_n^{\text{east}} - \Psi_n^{\text{west}}) \rangle}. \quad (1.18)$$

The first-order event plane has poor resolution. A full event plane analysis deals with twice the particle multiplicity as a sub-event plane analysis [37, 92]. Therefore we can approximate the full event plane resolution using

$$R_{\text{full}} \approx \sqrt{2} R_{\text{sub}}. \quad (1.19)$$

Figure 1.10 shows the 1st-order event plane resolution. This resolution improves at lower energies due to the strong v_1 signal near beam rapidities, which increasingly overlaps with the BBC acceptance as the beam energy drops.

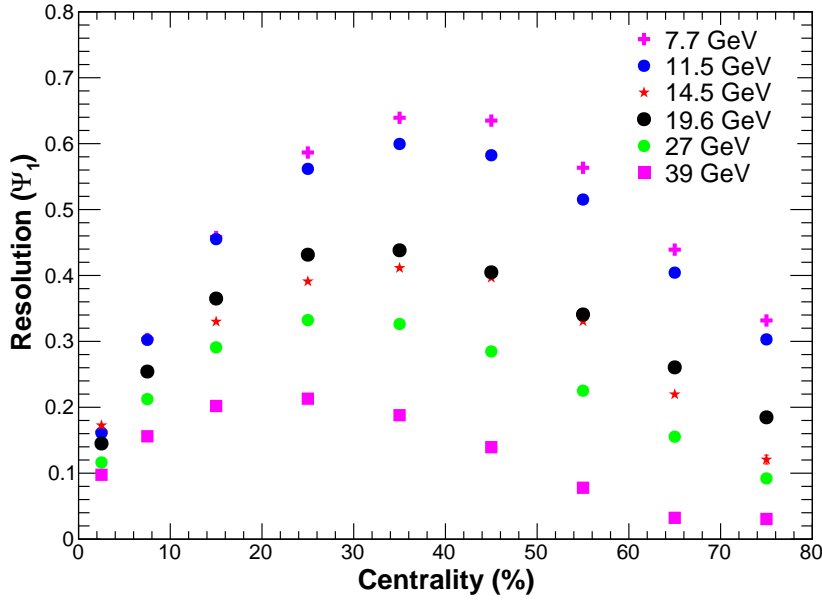


Figure 1.10: First order event plane resolution for all BES energies.

1.4 Directed Flow Measurements

The full event plane reconstructed using the east and west BBC is used to measure directed flow of particles produced in the TPC acceptance ($|y| \leq 1.0$). Eq. ?? shows the azimuthal distribution of produced particle with respect to the reaction plane. The first Fourier coefficient in this equation is the directed flow, v_1 . The directed flow for a given rapidity window, for all p_T , can be written in the form

$$v_1^{\text{obs}}(y_j, \forall p_T) = \langle \cos(\phi_i - \Psi_{\text{RP}}) \rangle \quad (1.20)$$

Here, “obs” means the observed directed flow before correcting for the reaction plane resolution. The angle brackets denote an average over all particles in all events, ϕ_i is the azimuthal

angle of particle i , and Ψ_{RP} is the first-order event plane. The true directed flow, corrected for event plane resolution, is

$$v_1 = \frac{v_1^{\text{obs}}}{R_1} \quad (1.21)$$

where R_1 is the first-order event plane resolution. Since, R_1 is a strong function of centrality, this step is implemented in fine centrality bins: 0-5%, 5-10%, 10-20%, 20-30%, 30-40%, 40-50%, 50-60%, 60-70% and 70-80%.

1.4.1 Directed Flow of Charged Particles – $\pi^\pm, K^\pm, p(\bar{p})$

Since $\pi^\pm, K^\pm, p(\bar{p})$ particles were directly identified from TPC and TOF, and no post processing is needed on PID signals, directed flow for these particles is calculated and stored in profile histograms as soon as each particle is identified.

1.4.2 Directed Flow of Neutral Strange Particles – $\Lambda, \bar{\Lambda}, K_S^0$

Directed flow calculation for $V0$ particles is not as simple as for charged particles. After identifying possible $V0$ candidates, it is necessary to remove the background to extract the signal. The steps to extract the signal and then calculate the directed flow for $V0$ particles are explained below.

1. Possible $V0$ candidates (signal+background) and mixed event background candidates are reconstructed as described in 1.2.2.
2. One-dimensional histograms containing invariant masses of both signal+background and background are stored in two separate, three-dimensional arrays, where the three array dimensions are centrality, rapidity, and $\phi - \Psi_{\text{RP}}$. Nine centrality bins span the

centrality interval 0-80%, 10 rapidity bins cover $|y| \leq 1.0$, and 30 bins of $\phi - \Psi_{\text{RP}}$ extend over $[0 - 2\pi]$.

Figure 1.11 shows a two-dimensional histogram of invariant mass and $\phi - \Psi_{\text{RP}}$ for Λ at 30-40% centrality and at $0.2 < y \leq 0.4$, based on Au+Au collisions at 19.6 GeV. The plot on the left shows the signal and background, while on the right is the normalized mixed-event background.

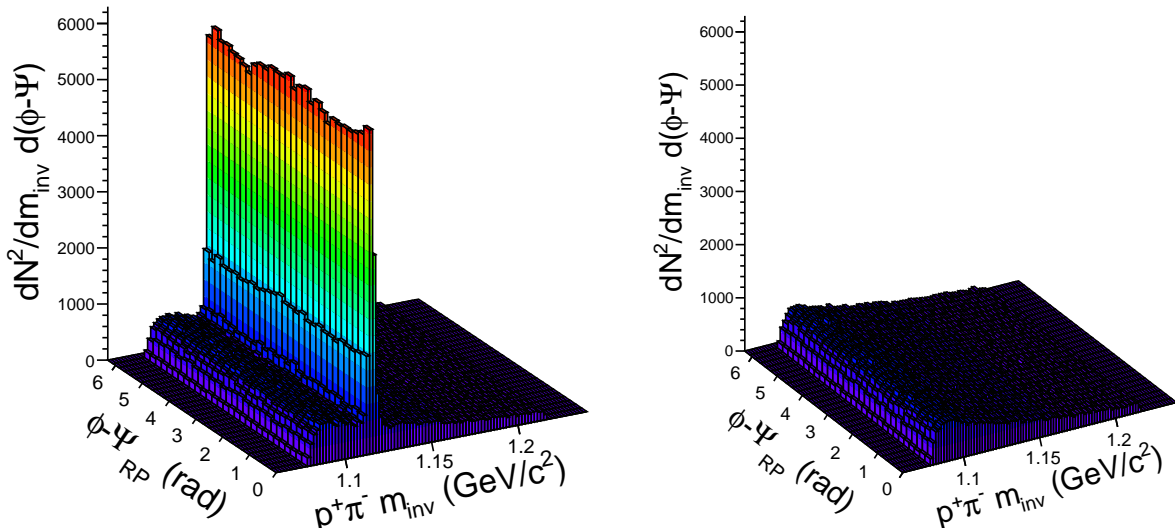


Figure 1.11: Histogram of signal+background (left) and normalized mixed-event background (right) for Λ as a function of invariant mass and $\phi - \Psi_{\text{RP}}$. These histograms are for 30-40% centrality Au+Au collisions at $\sqrt{s_{\text{NN}}} = 19.6$ GeV, with rapidity $0.2 < y \leq 0.4$.

3. The available dataset is too large to process all the events at once. This requires the data to be split into groups, each processed separately. At the end, to properly estimate the signal to background, all the groups are combined.

4. For each bin defined in step two above, the V_0 signal is extracted by removing the background. Then the yield is the integral of entries in the defined mass window. For $\Lambda(\bar{\Lambda})$ the mass is $1.1157 \pm 0.007 \text{ GeV}/c^2$ and for K_S^0 , the mass is $0.496 \pm 0.024 \text{ GeV}/c^2$, which are chosen to agree with values published by the Particle Data Group [86, 87].
5. For each centrality bin (c_i) and each rapidity bin (y_j) for all p_T , directed flow is calculated using equation 1.22:

$$v_1(c_i, y_j, \forall p_T) = \frac{\sum_{k=0}^{29} dn_k \left(\frac{\cos(\phi - \Psi_{\text{RP}})_k}{R_1^i} \right)}{\sum_{k=0}^{29} dn_k} \quad (1.22)$$

where R_1^i is the event plane resolution for the i^{th} centrality bin, and dn_k is the yield in the k^{th} bin of $\cos(\phi - \Psi_{\text{RP}})$.

1.4.3 Systematic Uncertainties

In this section, I discuss possible errors in v_1 calculations due to systematic uncertainties, and explain how the systematic uncertainties are estimated. A detector that is non-symmetric about the along the beam axis can introduce systematic error in v_1 calculations [93]. We have neglected possible error from this type of asymmetry since the STAR detector has desired east-west symmetry for the TPC, TOF and BBC detectors used in this analysis. The large pseudorapidity gap between BBC and TPC allows us to neglect the non-flow contribution in v_1 calculations [37, 94].

Another possible source of systematic error is from the event plane calculation. The number of track hits in BBC tiles and the number of tracks used to reconstruct the event plane can affect the BBC event plane resolution. Therefore, event and track quality cuts can

influence the event plane resolution. Directly identifying the systematic error associated with event plane calculations is very challenging. So we estimate the systematic uncertainty by assuming that the difference between the two event plane flattening techniques, the shifting method and the ψ method [95, 96], provides a rough estimate of the systematic uncertainty. This source of systematic error is estimated as less than 1% [81].

v_1 is a measure of the relative yield in small bins of $(\phi - \Psi)$. The assumption here is that the efficiency is constant as a function of centrality and as a function of the angle relative to Ψ . The results are not explicitly corrected for feed-down, although the systematic effect from varying DCA cuts (see below) partially takes care of the contributions from feed-down. In addition, previous studies [97] show that feed-down is significant for pions below $p_T \sim 0.4$ GeV/ c , while for other particles, feed-down corrections are negligible.

In addition, different p_T cuts are also studied, but such variations are not considered to contribute to the systematic error. Any experimental or theoretical analysis that is compared with the present results ought to use exactly the same p_T selection. A linear fit is used to find the slope of dv_1/dy , for the rapidity range $|y| \leq 0.8$. The fit range was varied to $|y| \leq 0.6$ in order to test sensitivity to the fit, but again, for the same reason as mentioned immediately above, this variation does not contribute to the final systematic error.

1.4.3.1 Detector Acceptance and Efficiency

Point-by-point systematic errors on parameters used for event selection, track selection, particle identification and topological selections are studied. Most cuts were varied $\pm 20\%$ from the reference values. Some special cuts don't follow the $\pm 20\%$ guideline. For example, I use zero for the lower value of the $\frac{n_{\text{Hits}}}{n_{\text{HitsPossible}}}$ cut, to check the full effect of the cut in the analysis. For all systematic checks, the various cuts are changed one at a time. Next,

I explain the procedure followed to identify the point-by-point systematic error using the $\Lambda(\bar{\Lambda})$ as an example:

1. Each cut is varied +20% and -20% from the default value, which gives a minimum and maximum on either side of the default value.
2. Table 1.4 shows the systematic cuts, and minimum and maximum values used for event and track quality selection for Λ .
3. The last column in this table is a unique identification number assigned to each systematic cut to identify the minimum and maximum cut in the plots that follow.
4. Similarly, Table 1.5 shows $V0$ topological cuts and variations used for systematics.
5. For each variation, rms values are found. There are 26 options, but some identification numbers are not assigned.

$$\text{RMS} = \sqrt{\frac{1}{2} \sum_{i=\text{min,max}} (y_i - y_{\text{default}})^2} \quad (1.23)$$

6. Then the final systematic error is calculated using

$$\text{systematic error} = \sqrt{\sum_{j=0}^N \text{RMS}_j^2} \quad (1.24)$$

where N = the total number of cut variations used for the systematic study.

7. Similarly, Tables 1.6 and 1.7 describe the K_S^0 systematic cuts. Tables 1.8 and 1.9 refer to proton and pion systematic cuts.

Cut	Default	Minimum	Maximum	Cut Number
Event				
V_z	50	40	60	1,2
Track				
Proton nHits	15	12	18	3,4
Proton $\frac{\text{nHits}}{\text{nHitsPossible}}$	0.52	0.0	0.60	5,6
Proton $n\sigma$	3.0	2.0	3.25	7,8
Proton mass ²	$0.5 \leq m^2 \leq 1.5$	$0.8 \leq m^2 \leq 1.0$	-	9
Pion nHits	15	12	18	11,12
Pion $\frac{\text{nHits}}{\text{nHitsPossible}}$	0.52	0.0	0.60	13,14
Pion $n\sigma$	3.0	2.0	3.25	15,16
Pion mass ²	$0.017 - 0.013 \times p \leq m^2 \leq 0.04$	$-0.01 \leq m^2 \leq 0.1$	-	17

Table 1.4: Minimum and maximum event and track cuts used for systematic study of $\Lambda(\bar{\Lambda})$. The cut number is a unique identifier assigned to each minimum and maximum cut value, used later to identify that variation in the plots. All lengths are in centimeters, all momenta are in GeV/c and all masses are in GeV/c^2 .

V0 Cuts		$\Lambda(\bar{\Lambda})$							Cut Number								
		Proton & Pions have TOF		Only Protons have TOF		Only for Pions have TOF		Neither has TOF		Cut Number							
V0 p_T	$0.4 \leq p_T \leq 5.0$				$ p < 2.8 \& 0.4 \leq p_T \leq 2.0$					19							
DCA Proton to PV >0.1	Default	Min 0.80	>0.15	0.12	>0.5	0.4	>0.6	0.48	(min)25								
		Max 0.12		0.18		0.6		0.72	(max)26								
DCA Pion to PV >0.7	>0.7	0.56	>0.8	0.64	>1.5	1.2	>1.7	1.36	27								
		0.84		0.96		1.8		1.24	28								
DCA V0 to PV 1.3	1.3	1.04	>1.2	0.96	>0.75	0.6	>0.75	0.6	21								
		1.56		1.44		0.9		0.9	22								
Decaylength >2.0	>2.0	1.6	>2.5	2.0	>3.5	2.8	>4.0	3.2	23								
		2.4		3.0		4.2		4.8	24								
DCA daughters	<1.00				0.8				29								
					1.2				30								

Table 1.5: Minimum and maximum p_T , V0 and decay daughter track cuts used to estimate systematic errors for $\Lambda(\bar{\Lambda})$. The cut number is a unique identifier assigned to each minimum and maximum cut, used later to identify that variation in the plots. All lengths are in centimeters, all momenta are in GeV/c and all masses are in GeV/c^2 .

Cut	Default	Minimum	Maximum	Cut Number
Event				
V_z	50	40	60	1,2
Track				
Pion nHits	15	12	18	3,4
Pion $\frac{\text{nHits}}{\text{nHitsPossible}}$	0.52	0.0	0.6	5,6
Pion $n\sigma$	3.0	2.0	3.25	7,8

Table 1.6: Minimum and maximum event and track cuts used to estimate systematic errors for K_S^0 . The cut number is a unique identifier assigned to each minimum and maximum cut, used later to identify that variation in the plots. All lengths are in centimeters.

V0	K_S^0	Cut Number	
		Independent of TOF	Cut Number
$V0\ p_T$	$0.4 \leq p_T \leq 5.0$	$1.6 \leq p \& 0.2 \leq p_T$	9
		-	-
DCA pions to PV	> 0.7	0.56	11
		0.84	12
DCA V0 to PV	> 0.8	0.64	13
		0.96	14
Decay length	> 3.0	2.4	15
		3.6	16
DCA Daughters	< 1.0	0.8	17
		1.2	18

Table 1.7: Minimum and maximum p_T , V0 and decay daughter track cuts used to estimate systematic errors for K_S^0 . The cut number is a unique identifier assigned to each minimum and maximum cut, used later to identify that variation in the plots. All lengths are in centimeters, and all momenta are in GeV/c .

Cut	Default	Minimum	Maximum	Cut Number
Event				
V_z	50	40	60	1,2
Track				
nHits	15	12	18	3,4
$\frac{n\text{Hits}}{n\text{HitsPossible}}$	0.52	0.00	0.6	5,6
$n\sigma$	2.0	1.6	2.4	7,8
mass^2	$0.8 < m^2 < 1.0$	$0.72 < m^2 < 1.1$	$0.88 < m^2 < 0.9$	9,10
DCA	3.0	2.4	3.6	11,12
Momentum	$2.8 > p \& 0.4 \leq p_T \leq 2.0$	$3.36 > p \& 0.32 \leq p_T \leq 2.4$	$2.24 > p \& 0.48 \leq p_T \leq 1.6$	13,14

Table 1.8: Minimum and maximum event and track cuts used to estimate systematic errors for protons. The cut number is a unique identifier assigned to each minimum and maximum cut, used later to identify that variation in the plots. All lengths are in centimeters, all momenta are in GeV/c and all masses are in GeV/c^2 .

Cut	Default	Minimum	Maximum	Cut Number
Event				
V_z	50	40	60	1,2
Track				
nHits	15	12	18	3,4
$\frac{n\text{Hits}}{n\text{HitsPossible}}$	0.52	0.00	0.6	5,6
$n\sigma$	2.0	1.6	2.4	7,8
pion mass 2	$-0.01 < m^2 < 0.1$	$-0.005 < m^2 < 0.05$	$-0.015 < m^2 < 0.15$	9,10
kaon mass 2	$0.2 < m^2 < 0.35$	$0.2 < m^2 < 0.30$	$0.18 < m^2 < 0.4$	9,10
DCA	3.0	2.4	3.6	11,12
Momentum	$2.8 > p \& 0.4 \leq p_T \leq 2.0$	$3.36 > p \& 0.32 \leq p_T \leq 2.4$	$2.24 > p \& 0.48 \leq p_T \leq 1.6$	13,14

Table 1.9: Minimum and maximum events cuts used to estimate systematic errors for pions and kaons. The cut number is a unique identifier assigned to each minimum and maximum cut, used later to identify that variation in the plots. All lengths are in centimeters, all momenta are in GeV/c and all masses are in GeV/c^2 .

Chapter 2

Experimental Results

This chapter presents rapidity-dependent directed flow and centrality-dependent directed flow measurements for all BES energies. Rapidity-dependent directed flow, $v_1(y)$, is presented for particle types Λ , $\bar{\Lambda}$, K_S^0 and K^\pm . Then the centrality dependence of directed flow is presented for particles types p , Λ , π^\pm , K_S^0 and K^\pm . Theoretical model calculations are already presented in Chapter ???. This chapter focuses purely on the experimental results and observations.

2.1 V0 Invariant Mass Distributions

The invariant mass distribution of Λ baryons is shown in Figure 2.1. It shows the signal + background distribution, and the estimated background distribution from the mixed event technique, for the beam energy 11.5 GeV, for 10-40% centrality Au+Au collisions. Similarly, Figure 2.2 shows the invariant mass distribution for K_S^0 . In directed flow calculations, to ensure that the signal + background $V0$ candidates and the background candidates differ only in the way intended, $V0$ candidates are grouped into fine bins of centrality, rapidity, and $(\phi - \Psi_{RP})$ as described in Section 1.4.2. Invariant mass distributions in 30 bins of $(\phi - \Psi_{RP})$,

for each particular centrality and rapidity bin, are shown in Figure 2.3 for Λ and in Figure 2.4 for K_S^0 . These are two typical cases, and all the other mass distributions look similar.

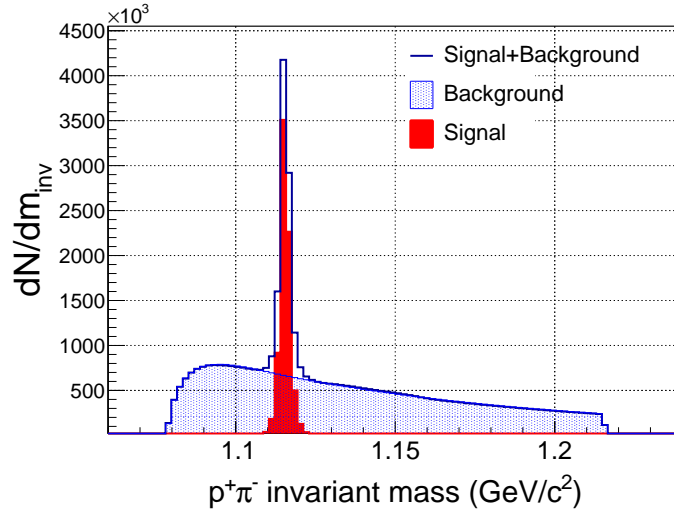


Figure 2.1: Invariant mass distribution of Λ for 10-40% centrality at $\sqrt{s_{NN}} = 11.5$ GeV. The solid blue histogram shows signal + background. The blue shaded area shows the mixed event background. The solid red area shows background-subtracted Λ candidates.

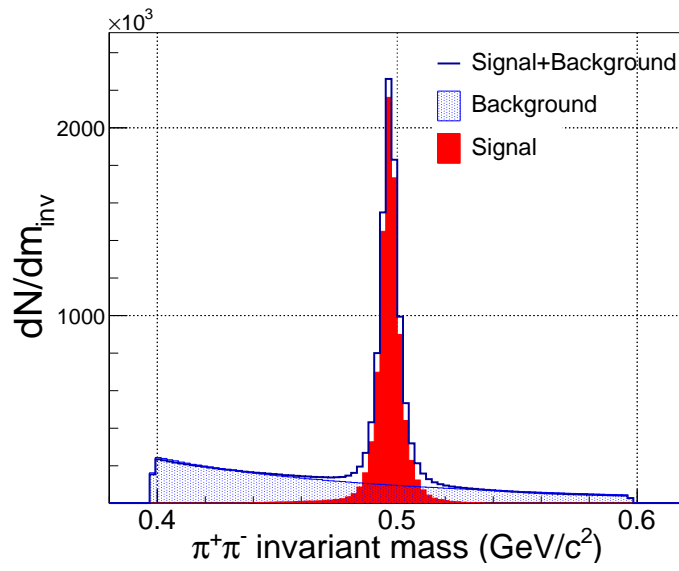


Figure 2.2: Invariant mass distribution of K_S^0 for 10-40% centrality at $\sqrt{s_{\text{NN}}} = 11.5 \text{ GeV}$. The solid blue histogram shows signal + background. The blue shaded area shows the mixed event background. The solid red area shows background-subtracted K_S^0 candidates.

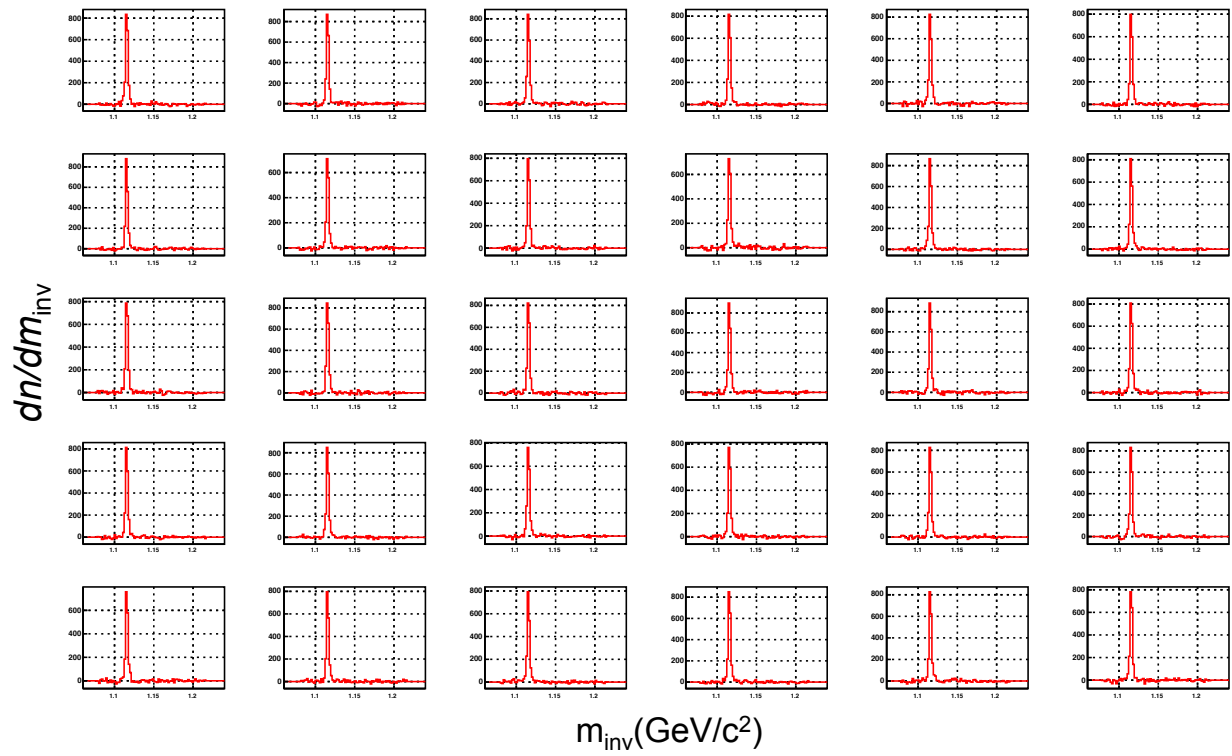


Figure 2.3: Λ invariant mass in thirty bins of $(\phi - \Psi_{\text{RP}})$ is shown for $-0.8 \leq y \leq -0.6$ and 30-40% centrality Au+Au collisions at a beam energy of 11.5 GeV.

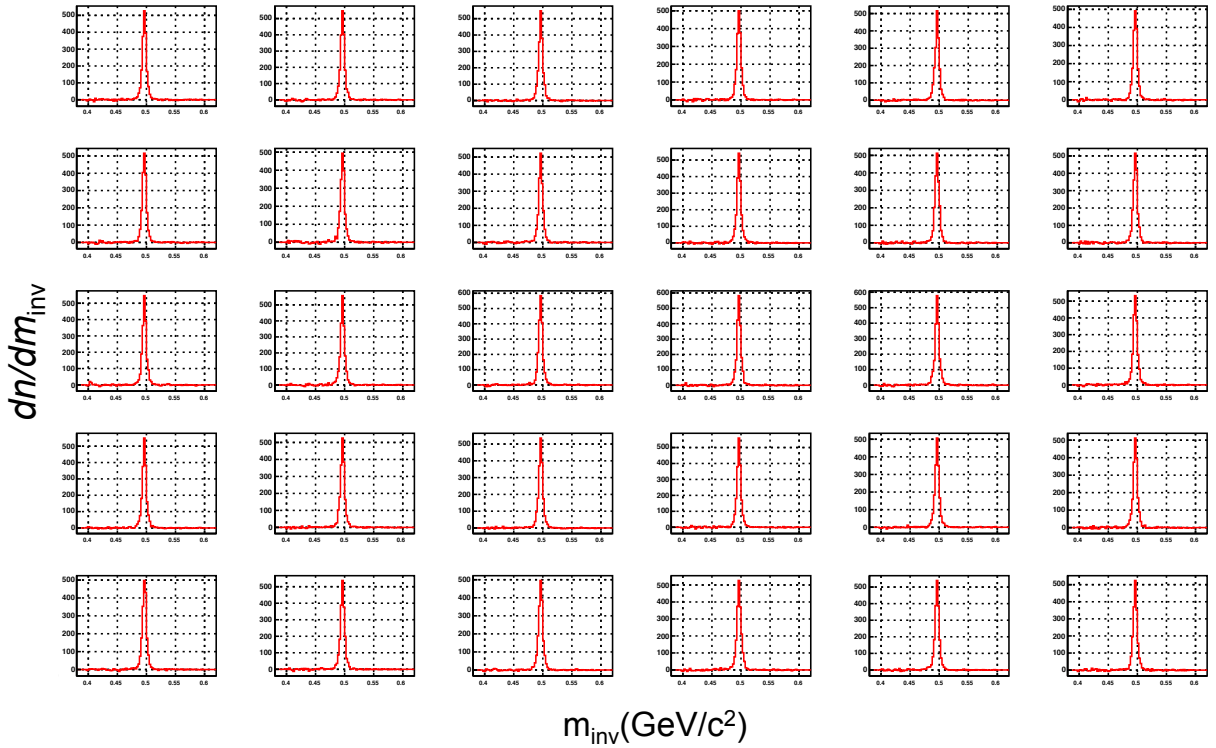


Figure 2.4: K_S^0 invariant mass in thirty bins of $(\phi - \Psi_{\text{RP}})$ is shown for $0.4 \leq y \leq 0.6$ and 20-30% centrality Au+Au collisions at a beam energy of 7.7 GeV.

2.2 Rapidity Dependence of Directed Flow

2.2.1 Intermediate Centrality Au+Au Collisions

Anisotropic flow is generally a maximum for intermediate centrality, and drops for both peripheral and central collisions. Because of limited statistics, the first directed flow study at BES energies [49] put its main focus on the intermediate centrality interval 10-40%. In this dissertation, the initial focus is on three key findings for intermediate centrality. First I present v_1 measurements from BES data recorded by the STAR detector. Second, I present similar v_1 calculations from events generated by the UrQMD model. Third, I present net-

particle analysis for protons, lambdas and kaons. The results from central (0-10%) and peripheral (40-80%) collisions are presented later in this chapter.

2.2.1.1 BES Data Analysis

Figure 2.5 shows v_1 as a function of rapidity (y) for all BES energies and for nine particle species at 10-40% centrality. Except for 14.5 GeV, results for 4 particle species, namely p , \bar{p} and π^\pm , are already published by STAR [49]. Because the 14.5 GeV energy data are now available, for completeness, the full set of data for p , \bar{p} and π^\pm are presented here. The top row shows results for protons. At 7.7 GeV, proton v_1 has positive slope, then becomes negative at 11.5 GeV, and remains negative and small for the rest of the BES energies. The sign of the v_1 slope is assigned according to a historical convention. Positive v_1 is defined, in a fixed target experiment, as the direction of projectile spectator fragments, which always undergo repulsive scattering in the reaction plane at relativistic energies. The next row shows results for Λ , where v_1 is very similar to proton v_1 . The third and fourth rows show results for \bar{p} and $\bar{\Lambda}$, which have the poorest statistics of the 9 species studied, especially at 7.7 GeV. These particles show negative and large v_1 for all BES energies. Rows five, six and seven show K^+ , K^- and K_S^0 , respectively. Directed flow of these particles remains negative for all BES energies. The last two rows are for charged pions, which also show negative slope for all BES energies.

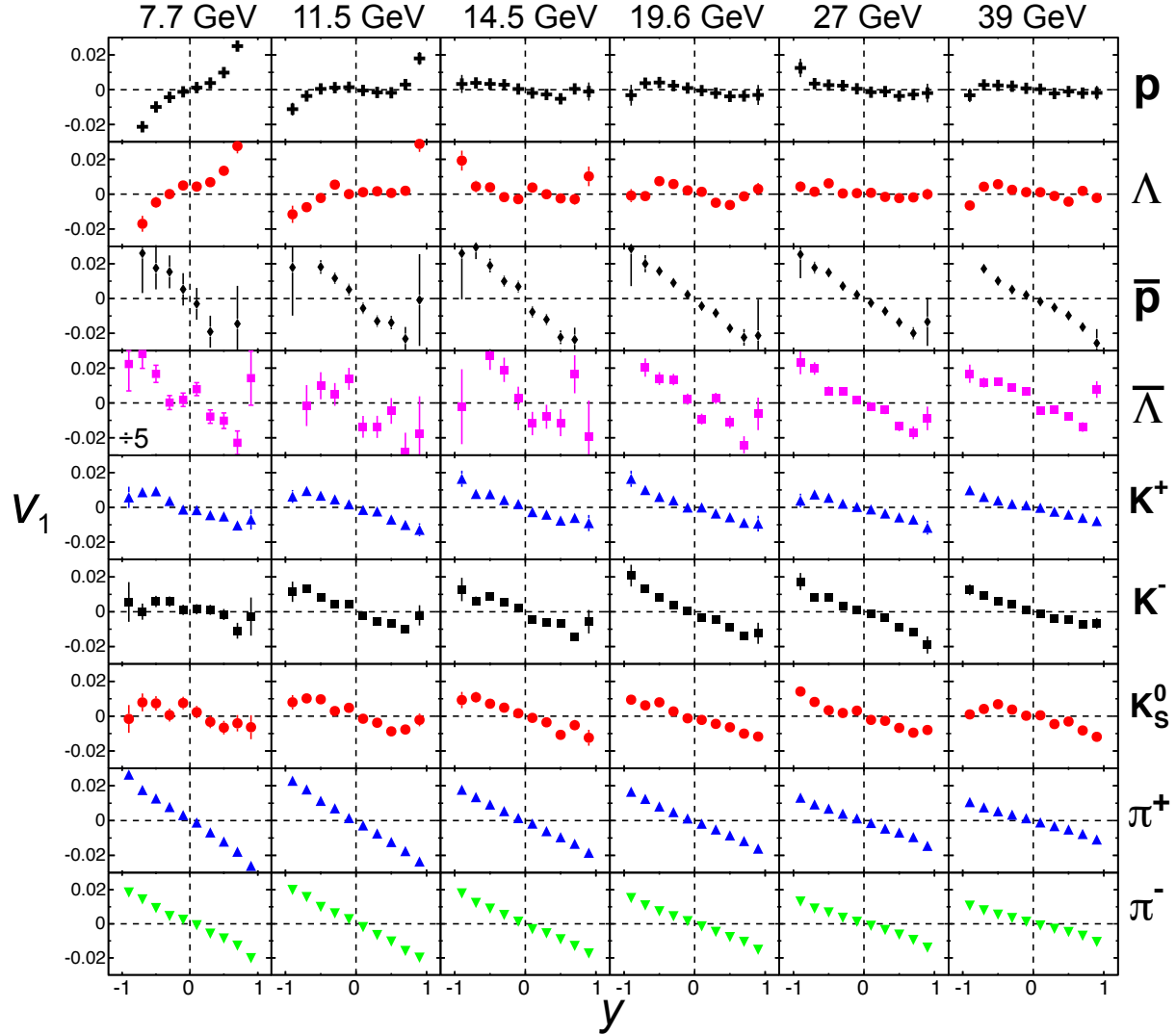


Figure 2.5: Directed flow (v_1) as a function of rapidity for p , Λ , \bar{p} , $\bar{\Lambda}$, K^\pm , K_s^0 and π^\pm for 10-40% centrality Au+Au collisions. Error bars are statistical. The v_1 magnitude is exceptionally large for $\bar{\Lambda}$ at 7.7 GeV, and therefore in that panel only, v_1 and its errors are divided by 5 to fit on the common vertical scale.

The strength of directed flow near midrapidity is quantified by the slope of $v_1(y)$. In this analysis, a linear fit to the data is carried out over the rapidity range $|y| \leq 0.8$. Throughout this dissertation, the term “ v_1 slope” is shorthand for $dv_1/dy|_{y \leq 0.8}$. In the previous STAR analysis of BES v_1 [49], a slightly different definition was used, namely, a cubic fit was carried

out as per $v_1(y) = Fy + Cy^3$, and the linear term F was defined as the v_1 slope. When statistics are good, this approach has the advantage of less sensitivity to the fit range. The disadvantage, and the reason for a different definition in the present dissertation, is that the cubic fit becomes unstable for rarer particle types, because of poorer statistics. The two methods give similar values for the slope when statistics are good, e.g., for protons and pions at energies above 14.5 GeV.

Figure 2.6 shows dv_1/dy for Λ , $\bar{\Lambda}$, p , \bar{p} and π^\pm , as a function of beam energy for 10-40% centrality. As discussed earlier, the v_1 slope for protons shows a positive slope at 7.7 GeV, then at 11.5 GeV it becomes close to zero. Above 11.5 GeV, the v_1 slope for protons remains negative. Protons show a statistically significant minimum in the v_1 slope, as predicted by models with a strong “softening” effect. Within statistical errors, Λ dv_1/dy shows similar results as for protons. Slopes for \bar{p} , $\bar{\Lambda}$ and π^\pm are all negative and large in magnitude compared to p and Λ , for all beam energies. \bar{p} and $\bar{\Lambda}$ are roughly consistent within statistical errors, except at 7.7 GeV, where dv_1/dy for $\bar{\Lambda}$ shows a large deviation from \bar{p} . Of course, both statistical and systematic errors are especially large for antibaryons at 7.7 GeV.

Figure 2.7 shows dv_1/dy versus beam energy for K^\pm and K_S^0 . The dv_1/dy for K^\pm and K_S^0 are negative and similar in magnitude to π^\pm at BES energies. Another noteworthy observation is that at all BES energies, dv_1/dy for K_S^0 is in between K^+ and K^- within errors.

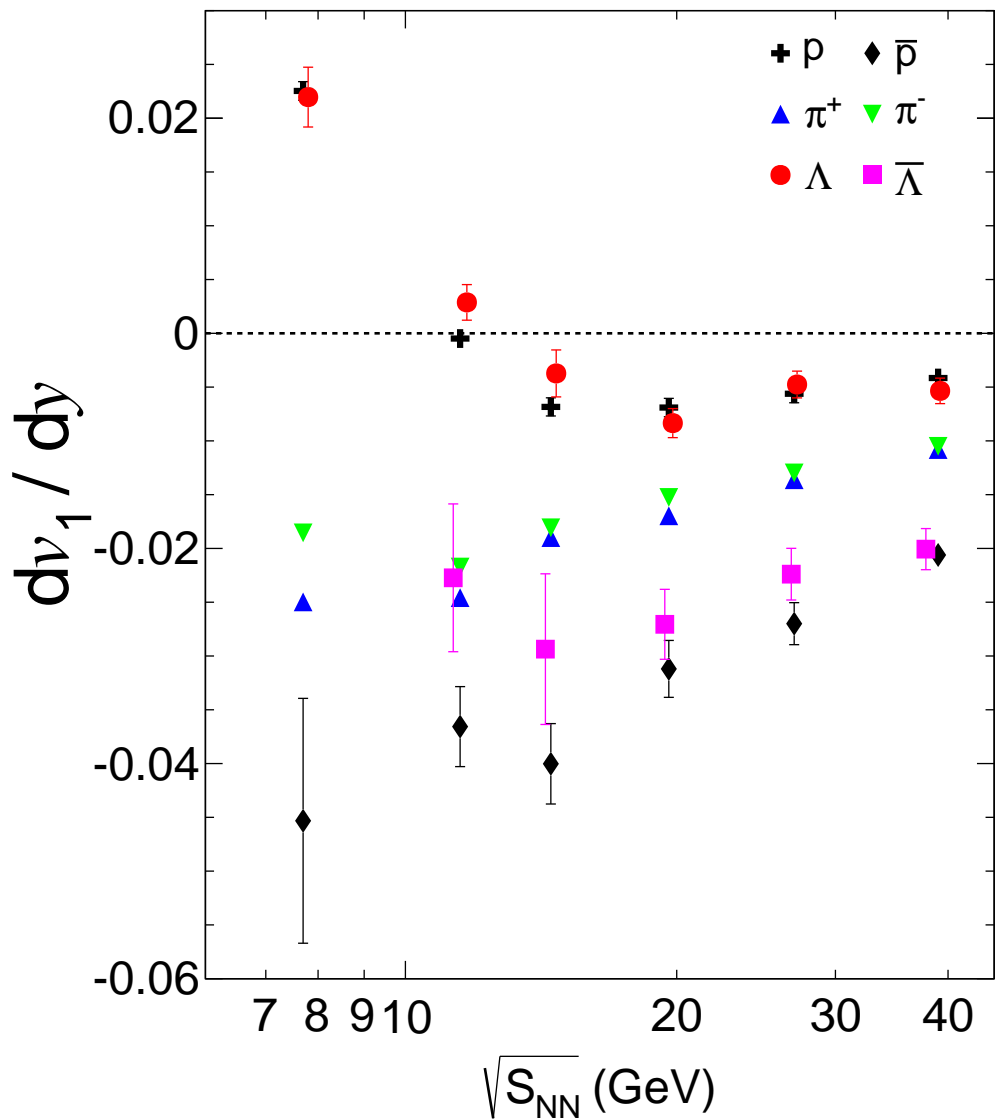


Figure 2.6: dv_1/dy near mid-rapidity as a function of beam energy for p , \bar{p} , π^\pm , Λ and $\bar{\Lambda}$ for 10-40% central Au+Au collisions. The dv_1/dy for $\bar{\Lambda}$ at 7.7 GeV is -0.13 ± 0.02 , which lies off-scale, below the lower end of the vertical axis. Error bars are statistical.

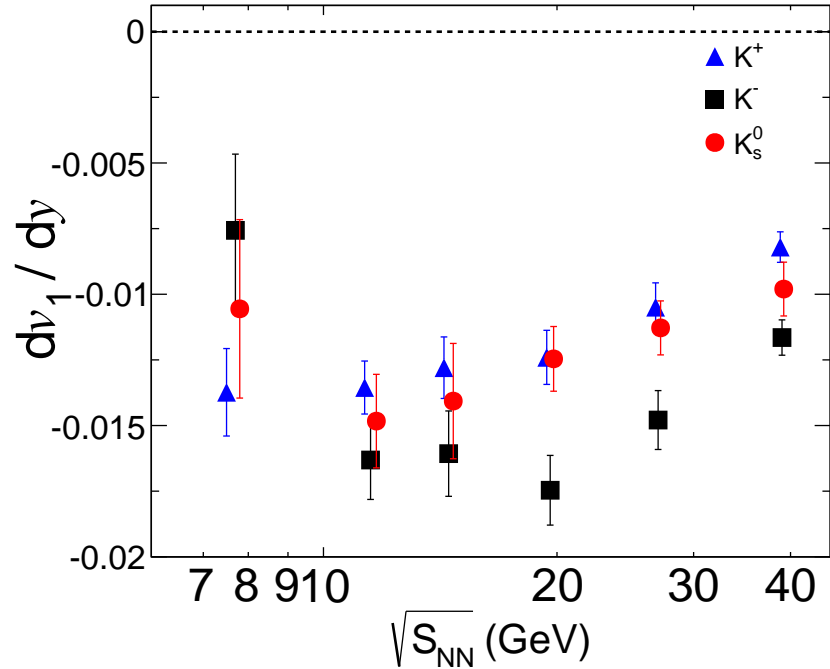


Figure 2.7: dv_1/dy near mid-rapidity as function of beam energy for K^+ , K^- and K_s^0 for 10-40% central Au+Au collisions. Error bars are statistical.

2.2.1.2 UrQMD Model Calculations

In this dissertation, I am using UrQMD version 3.3p2. Table 2.1 summarizes the available UrQMD event statistics, which were generated with default UrQMD settings. Particles are identified using the particle ID provided by UrQMD, without any p_T quality cuts applied. The centrality of UrQMD events is assigned with the aid of particle multiplicity, as in experiment.

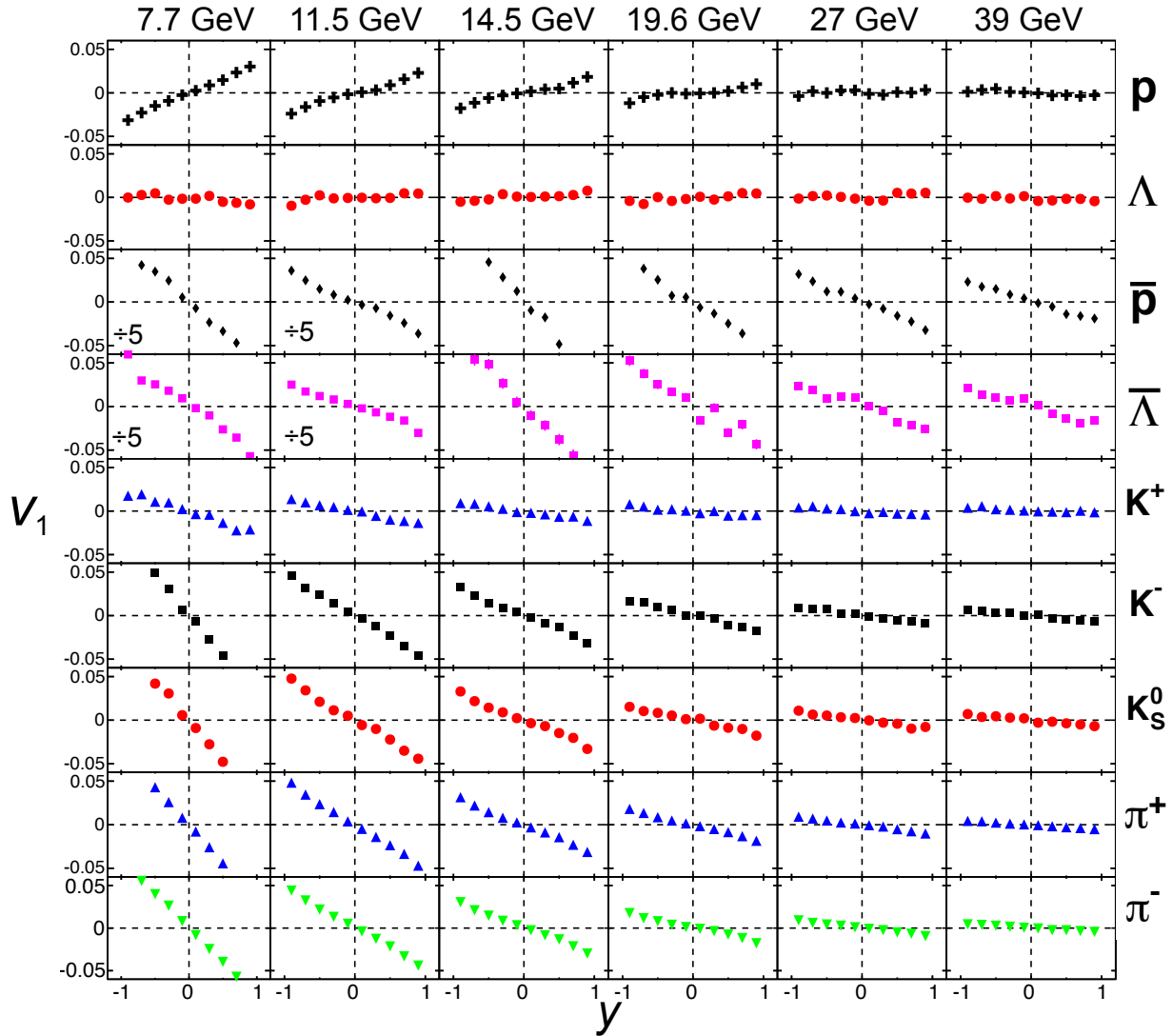


Figure 2.8: Directed flow as a function of rapidity for p , Λ , \bar{p} , $\bar{\Lambda}$, K^\pm , K_s^0 and π^\pm for 10-40% central UrQMD Au+Au collisions. Error bars are statistical. The v_1 magnitude is exceptionally large for \bar{p} and $\bar{\Lambda}$ at 7.7 and 11.5 GeV, and therefore for only for those four panels, v_1 and its errors are divided by 5 to fit on the common vertical scale.

Energy	UrQMD Events ($\times 10^6$)	Real Events ($\times 10^6$)
7.7	0.78	4
11.5	0.76	12
14.5	0.74	20
19.6	0.28	36
27	0.28	70
39	0.28	130

Table 2.1: Summary of the event statistics used in UrQMD simulations. For reference, real event statistics are also shown.

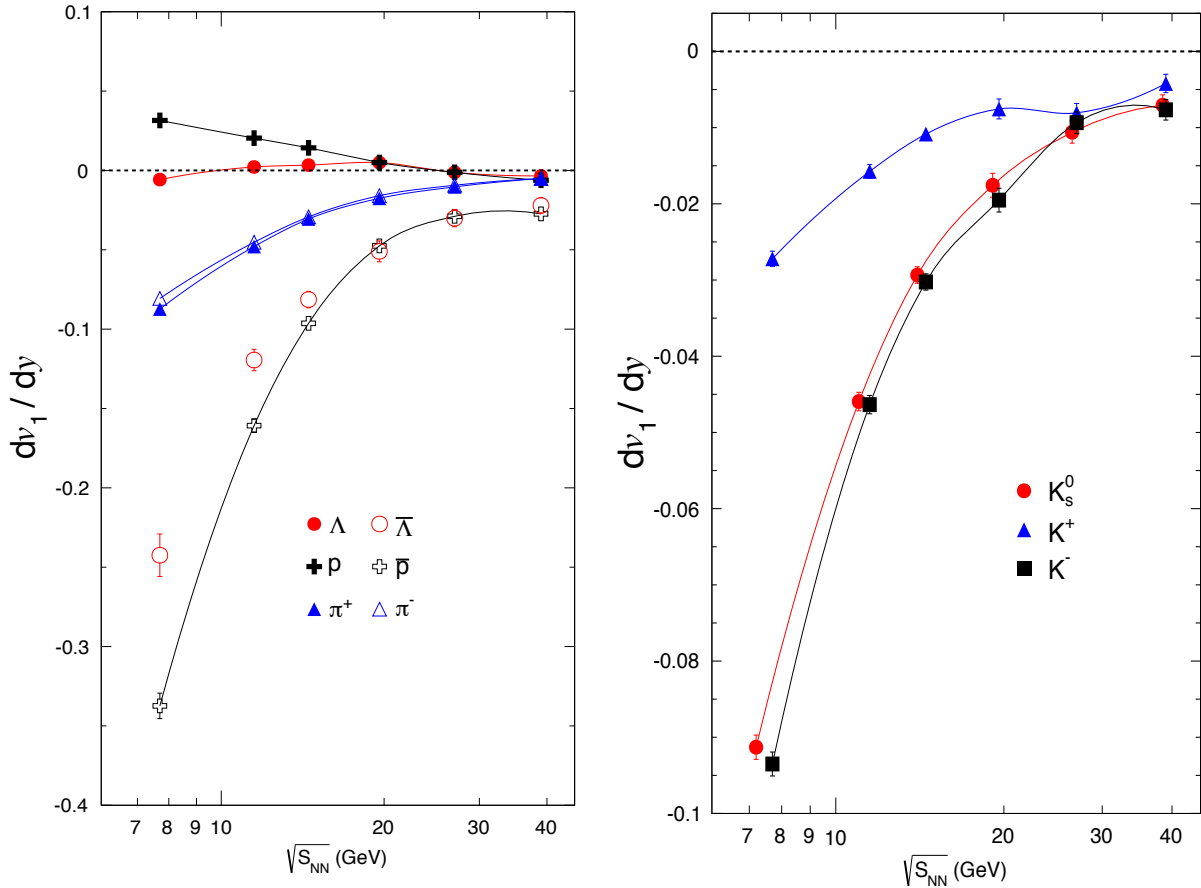


Figure 2.9: The left panel shows dv_1/dy near mid-rapidity as function of beam energy for p , \bar{p} , π^\pm , Λ and $\bar{\Lambda}$ from UrQMD events for 10-40% central Au+Au collisions. Similarly, the right panel is for K^\pm and K_S^0 . Error bars are statistical.

Figure 2.8 shows v_1 as a function of rapidity (y), from UrQMD events at all BES energies and for all nine particle species at 10-40% centrality. The left panel of Figure 2.9 shows dv_1/dy for Λ , $\bar{\Lambda}$, p , \bar{p} and π^\pm , as a function of beam energy for 10-40% centrality, while the right panel shows the same for K^\pm and K_S^0 . In general, UrQMD shows larger v_1 magnitude for all the particles and for all energies. For protons, dv_1/dy shows a sign change, but no minimum is observed as in the data. Λ shows nearly zero dv_1/dy for all energies, while $\bar{\Lambda}$ shows always a strongly negative dv_1/dy . Charged pions and kaons show negative slope for all BES energies, and the slope of K_S^0 is consistent with K^- for UrQMD events.

2.2.1.3 Systematic Uncertainty Study

A detailed explanation of the procedure for study of systematic uncertainties is given in Section 1.4.3. This section presents results from that systematic study. For example, at beam energies of 11.5 and 39 GeV, the systematic error in v_1 versus y is shown in Figures 2.10, 2.11, 2.12 and 2.13 for all nine particle types studied. For 11.5 GeV and the rest of the energies, \bar{p} and $\bar{\Lambda}$ show large systematic error. For the other particle species, systematic errors are comparable to statistical errors. For example, at beam energies of 11.5 and 39 GeV, the variation from the default dv_1/dy arising from various sources of systematic error are presented in Figure 2.14 for Λ , $\bar{\Lambda}$, and K_S^0 . Similarly, for the example of the beam energy of 11.5 GeV, systematic errors for particle types p , \bar{p} , π^\pm and K^\pm presented in Figure 2.14. A unique identifier called “cut number” is assigned to each source of possible systematic error to identify it in the graph. Cut number zero corresponds to the default (optimum) combination of quality cuts. In this study, the effect of varying p_T cuts from the default (optimum) value is also studied, but for reasons explained in Section 1.4.3, this source is not included as part of the total systematic error. The final systematic error and statistical error are indicated by a red data point at the far right side of Figures 2.14 and 2.15. For Λ and

$\bar{\Lambda}$, additional contributions from event and track quality cuts and from $V0$ vertex cuts are also separately studied. This study shows that a larger contribution to the final systematic error comes from event and track quality cuts compared to $V0$ vertex selection cuts.

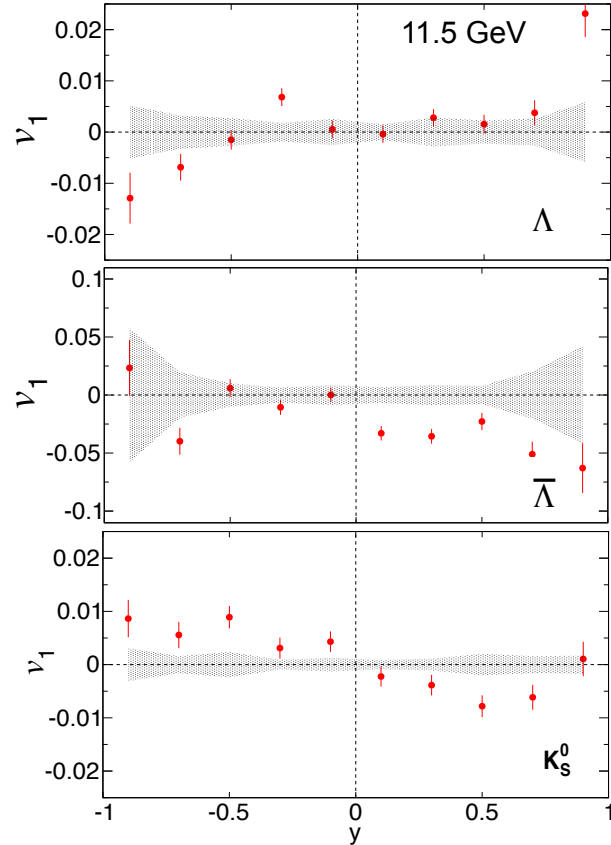


Figure 2.10: Error from systematic variations is shown by the shaded band for v_1 vs. y , for particles Λ , $\bar{\Lambda}$ and K_S^0 , in 10-40% central collisions at a beam energy of 11.5 GeV.

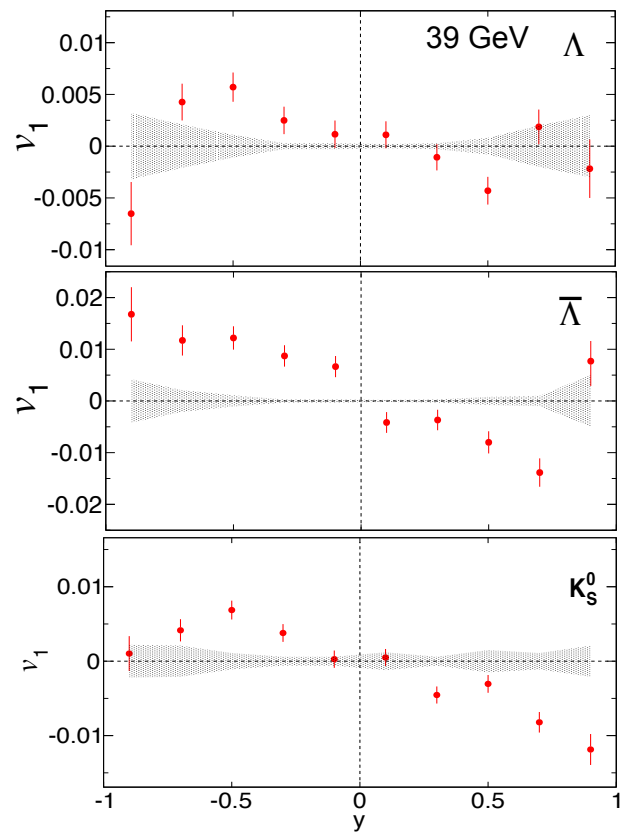


Figure 2.11: Error from systematic variations is shown by the shaded band for v_1 vs. y , for particles Λ , $\bar{\Lambda}$ and K_S^0 , in 10-40% central collisions at a beam energy of 39 GeV.

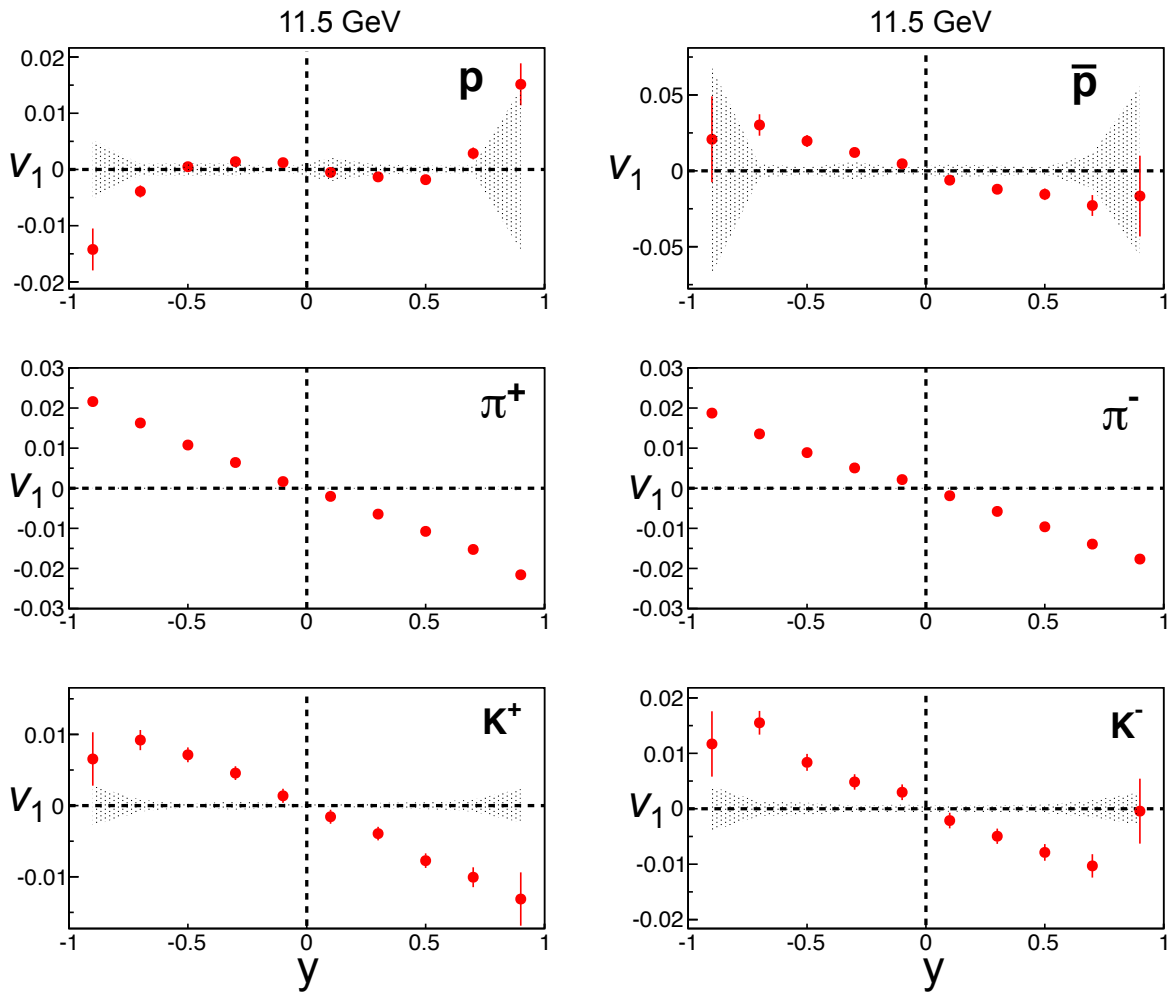


Figure 2.12: Error from systematic variations is shown by the shaded band for v_1 vs. y , for particles p , \bar{p} , π^\pm and K^\pm , in 10-40% central collisions at a beam energy of 11.5 GeV. The systematic error for π^\pm is small and is not visible on the scale of this plot.

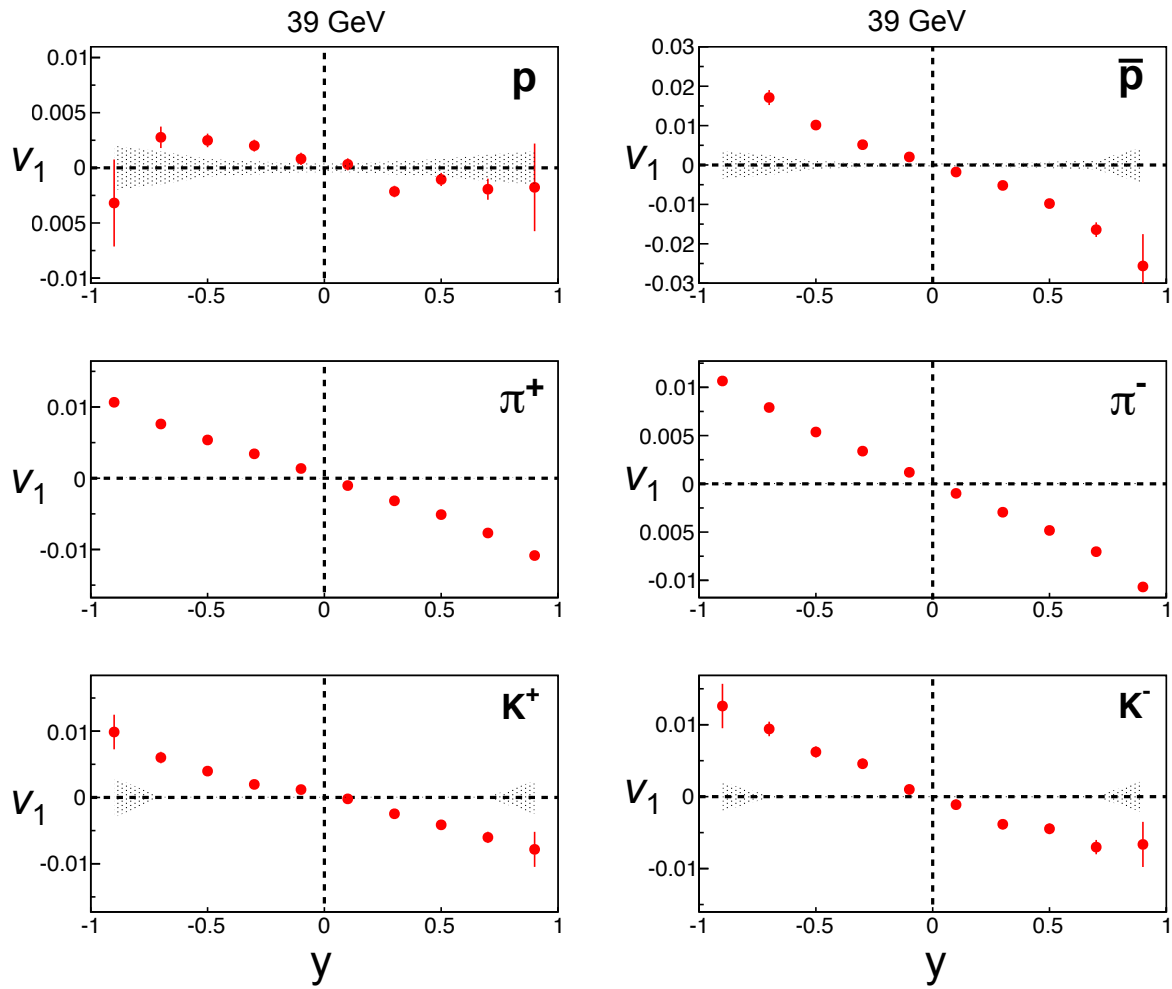


Figure 2.13: Error from systematic variations is shown by the shaded band for v_1 vs. y , for particles p , \bar{p} , π^\pm and K^\pm , in 10-40% central collisions at a beam energy of 39 GeV. The systematic error for π^\pm is small and is not visible on the scale of this plot.

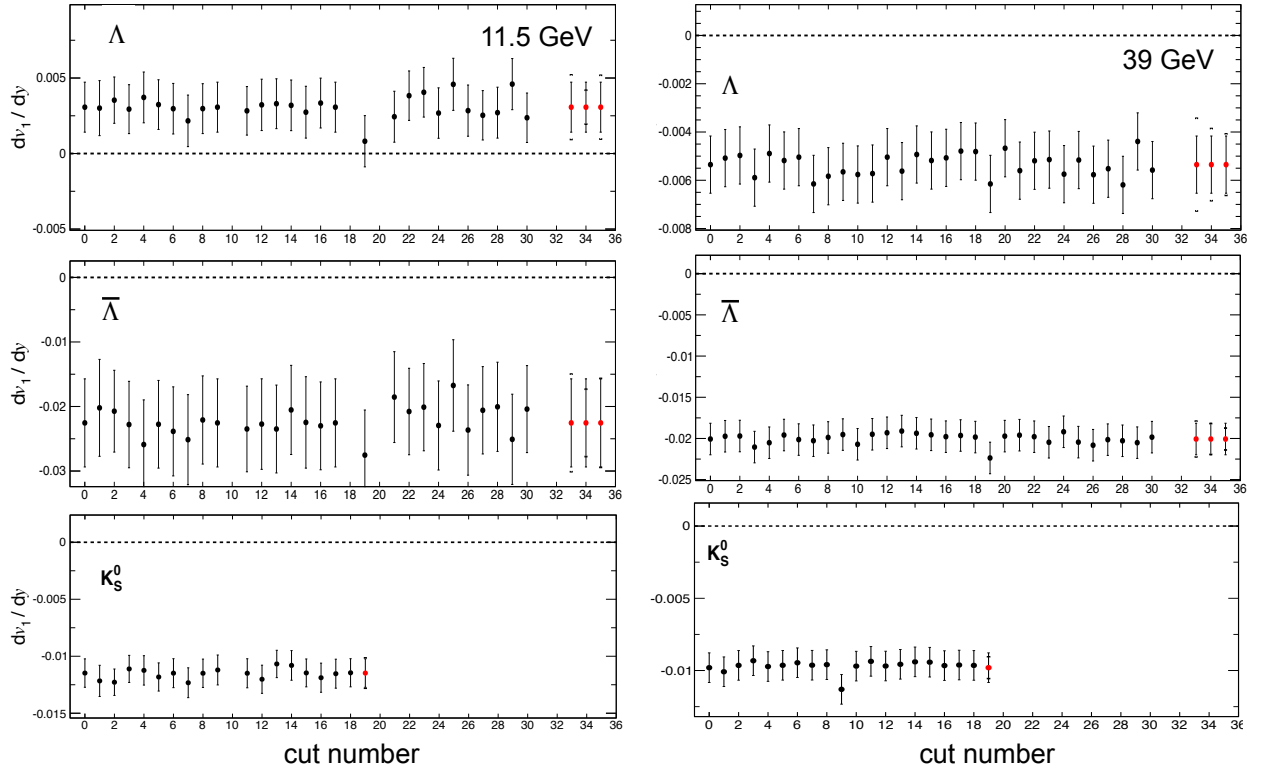


Figure 2.14: The effect from different sources of systematic error is shown for dv_1/dy from 10-40% central collisions at a beam energy of 11.5 GeV on left and of 39 GeV on right. The cut number is defined in Table 1.4 and 1.5 for Λ and $\bar{\Lambda}$ baryons, and in Table 1.6 and 1.7 for K_S^0 . For Λ and $\bar{\Lambda}$, cut number 33 is the final data point with systematic and statistical errors, cut number 34 corresponds to systematic errors from event and track quality cuts, and cut number 35 includes only $V0$ systematic errors. For K_S^0 , cut number 19 is the final data point with systematic and statistical errors.

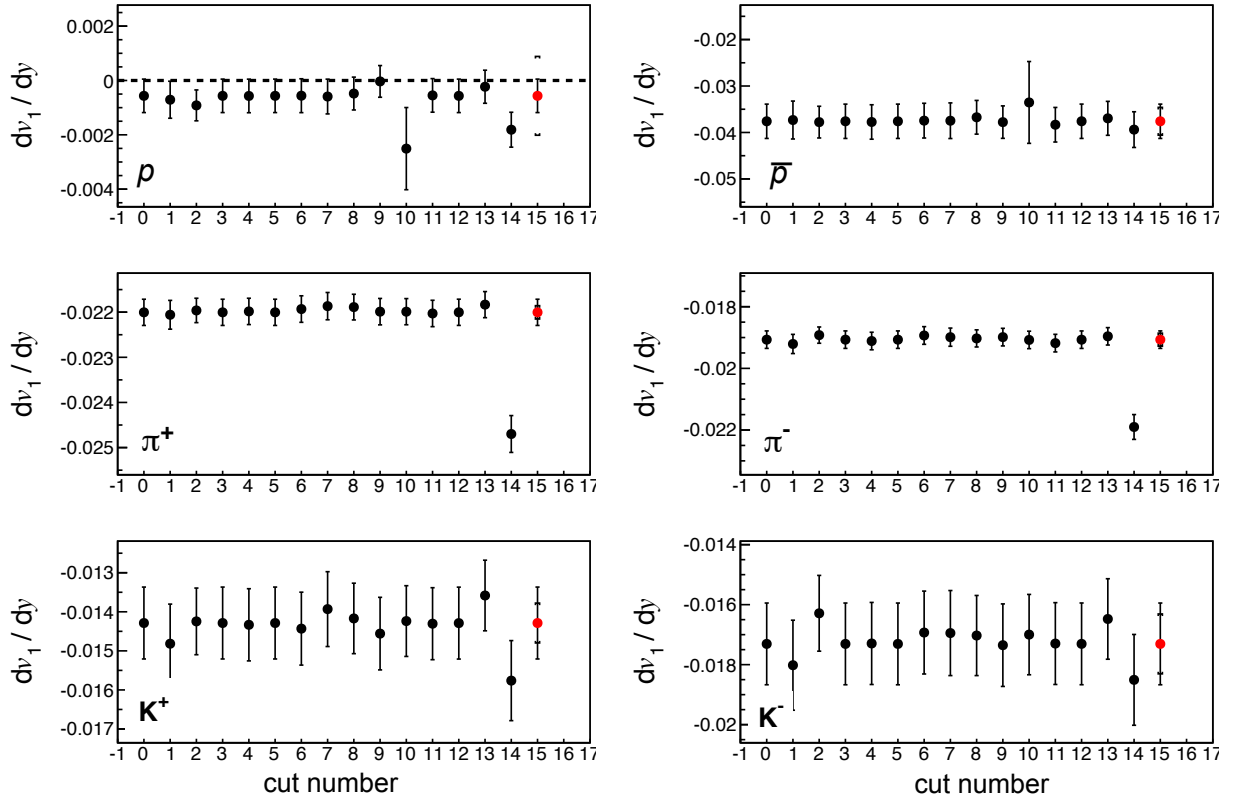


Figure 2.15: The effect from different sources of systematic error is shown for dv_1/dy from 10-40% central collisions at a beam energy of 11.5 GeV. The cut number is defined in Table 1.8 for p and \bar{p} , and in Table 1.9 for π^\pm and K^\pm . Cut number 15 is the final data point with systematic and statistical errors.

2.2.1.4 Net-Particle Directed Flow

Directed flow near midrapidity has contributions both from protons produced as baryon-antibaryon pairs in the hot participant zone, as well from protons associated with conserved baryon number transported from the initial-state nuclei towards midrapidity by the stopping process of the nuclear collision. We want to distinguish between these two distinct mechanisms, and a measurement of net-baryon flow would help us to do that. In our experiment, it is not possible to directly identify net baryons, and therefore net protons are used as a

proxy for net baryons. In order to roughly estimate the flow contribution associated with the transported baryon number, we hypothesize that quarks in antiprotons and in produced protons have roughly the same directed flow. This hypothesis is suggested by the observation that the measured v_1 for π^+ and π^- [49], for K^+ and K^- , for \bar{p} and $\bar{\Lambda}$ are very similar. Therefore, the following definition of net-proton v_1 is our best estimate of a proxy observable for the transported component,

$$[v_1(y)]_p = r(y)[v_1(y)]_{\bar{p}} + (1 - r(y)) [v_1(y)]_{\text{net-}p}, \quad (2.1)$$

where $r(y)$ is the rapidity-dependent ratio of observed antiprotons to protons. Then we define net- Λ and net-kaon v_1 using the same formula, with p and \bar{p} replaced by Λ and $\bar{\Lambda}$ for net- Λ flow and p and \bar{p} replaced by K^+ and K^- for net-kaon flow, respectively. Figure 2.16 shows net-proton, net- Λ and net-kaon results. The net-particle dv_1/dy results are consistent for protons and Λ s, but dv_1/dy for net kaons strongly deviates from the other two cases for beam energies less than 14.5 GeV. The reason for the latter pattern is not yet understood.

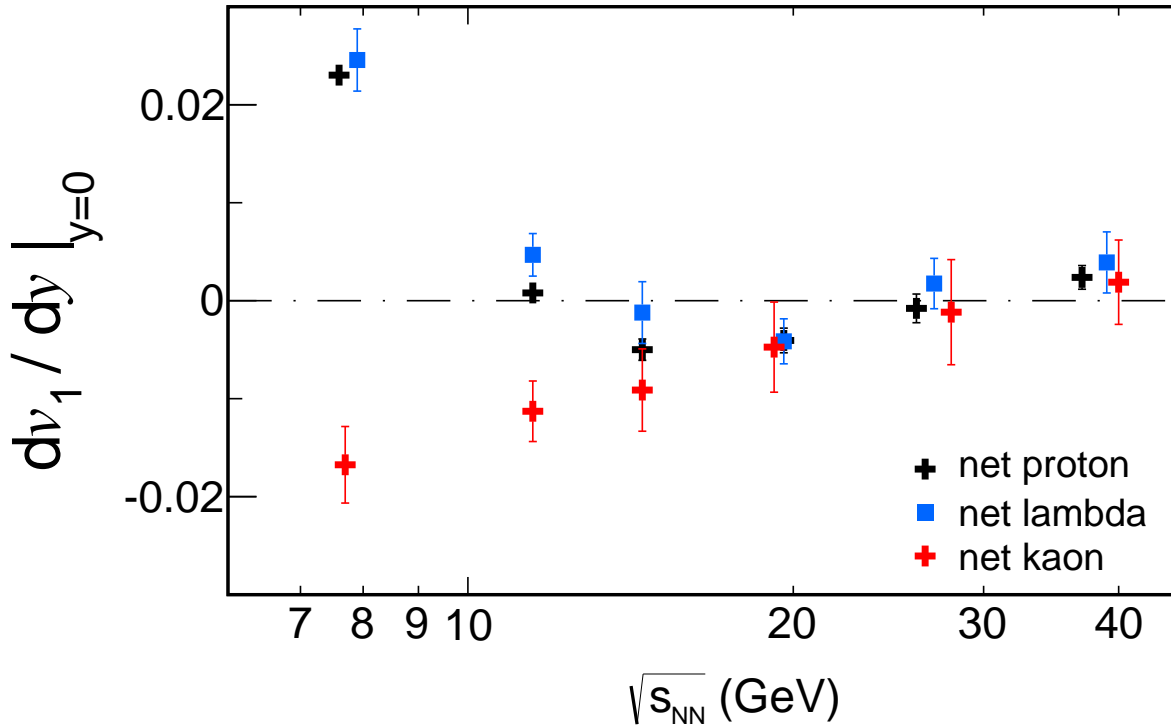


Figure 2.16: dv_1/dy near mid-rapidity at 10-40% centrality for net protons, net Λ s and net kaons.

2.2.1.5 Summary of Intermediate Centrality Results

Figure 2.17 shows the observed dv_1/dy as a function of beam energy as well as UrQMD calculations for p , Λ , \bar{p} , $\bar{\Lambda}$, and π^\pm at 10-40% centrality, with statistical and systematic errors. For p and Λ , UrQMD shows very poor agreement with data, especially at 19.6 GeV and below. UrQMD's v_1 slope for \bar{p} , $\bar{\Lambda}$, and π^\pm shows a qualitatively similar trend as data at higher energies, but strongly deviates at lower energies.

Figure 2.18 shows the same for particles K^\pm and K_s^0 . For K^\pm and K_s^0 , UrQMD's v_1 slope also shows a qualitatively similar trend as data at higher energies, but strongly deviates at lower energies.

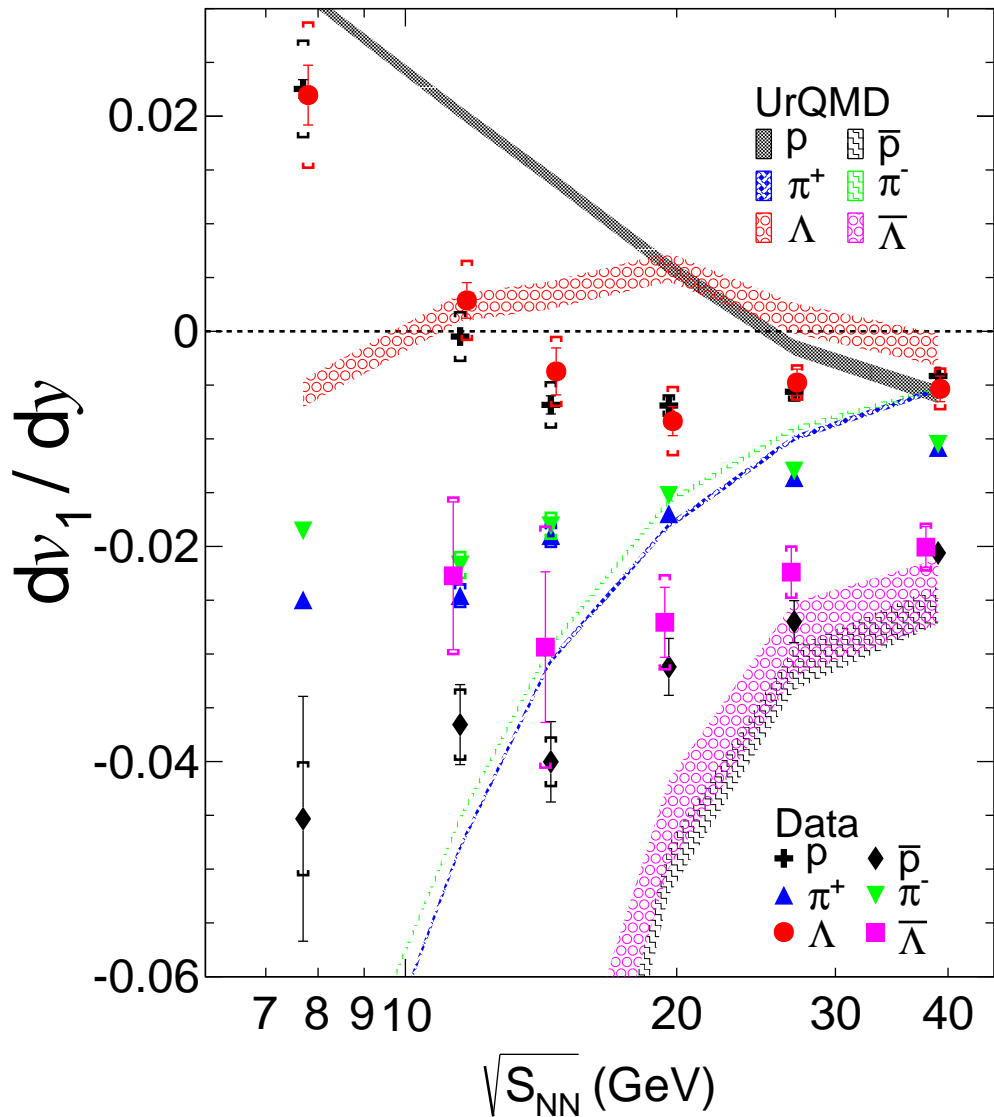


Figure 2.17: Slope of v_1 near mid-rapidity as a function of beam energy for protons, antiprotons, Λ , $\bar{\Lambda}$, and π^\pm for 10-40% central collisions. Solid data points show BES data and shaded bands show UrQMD calculations. The dv_1/dy for $\bar{\Lambda}$ at 7.7 GeV is -0.13 ± 0.02 , which lies off-scale, below the lower end of the vertical axis. Error bars are statistical, while caps show systematic errors.

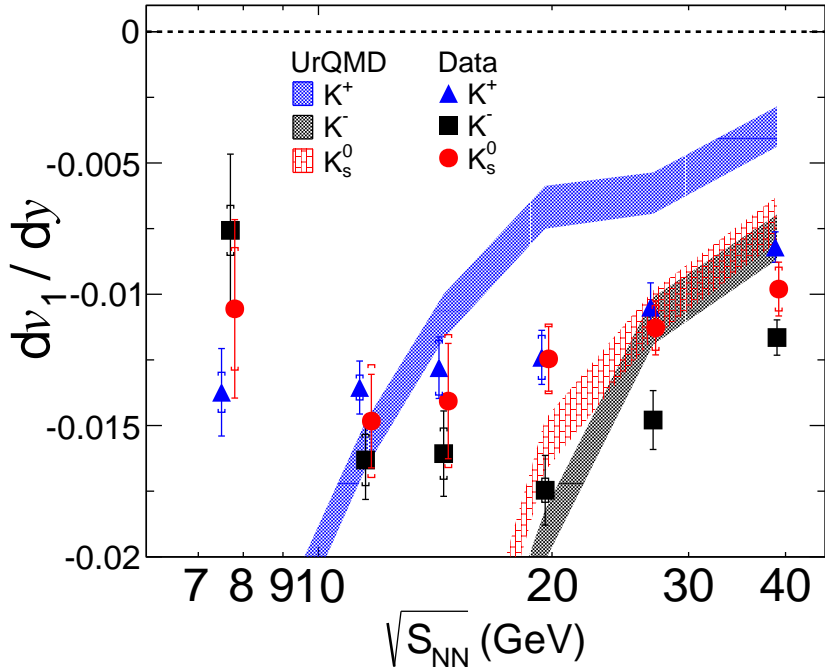


Figure 2.18: Slope of v_1 near mid-rapidity as a function of beam energy for K^\pm and K_s^0 for 10-40% central collisions. Solid data points show BES data and shaded bands show UrQMD calculations. Error bars are statistical, while caps show systematic errors.

2.2.2 Peripheral and Central Au+Au Collisions

Rapidity-dependent v_1 is shown in Figure 2.19 for central (0-10%) collisions, and in Figure 2.20 for peripheral (40-80%) collisions. In general, 0-10% centrality shows small and negative dv_1/dy compared to intermediate centrality. For peripheral collisions, in general the magnitude of dv_1/dy is larger than at intermediate centrality. Statistics for \bar{p} and $\bar{\Lambda}$ at 7.7 and 11.5 GeV are especially low, so a clear trend in dv_1/dy cannot be seen.

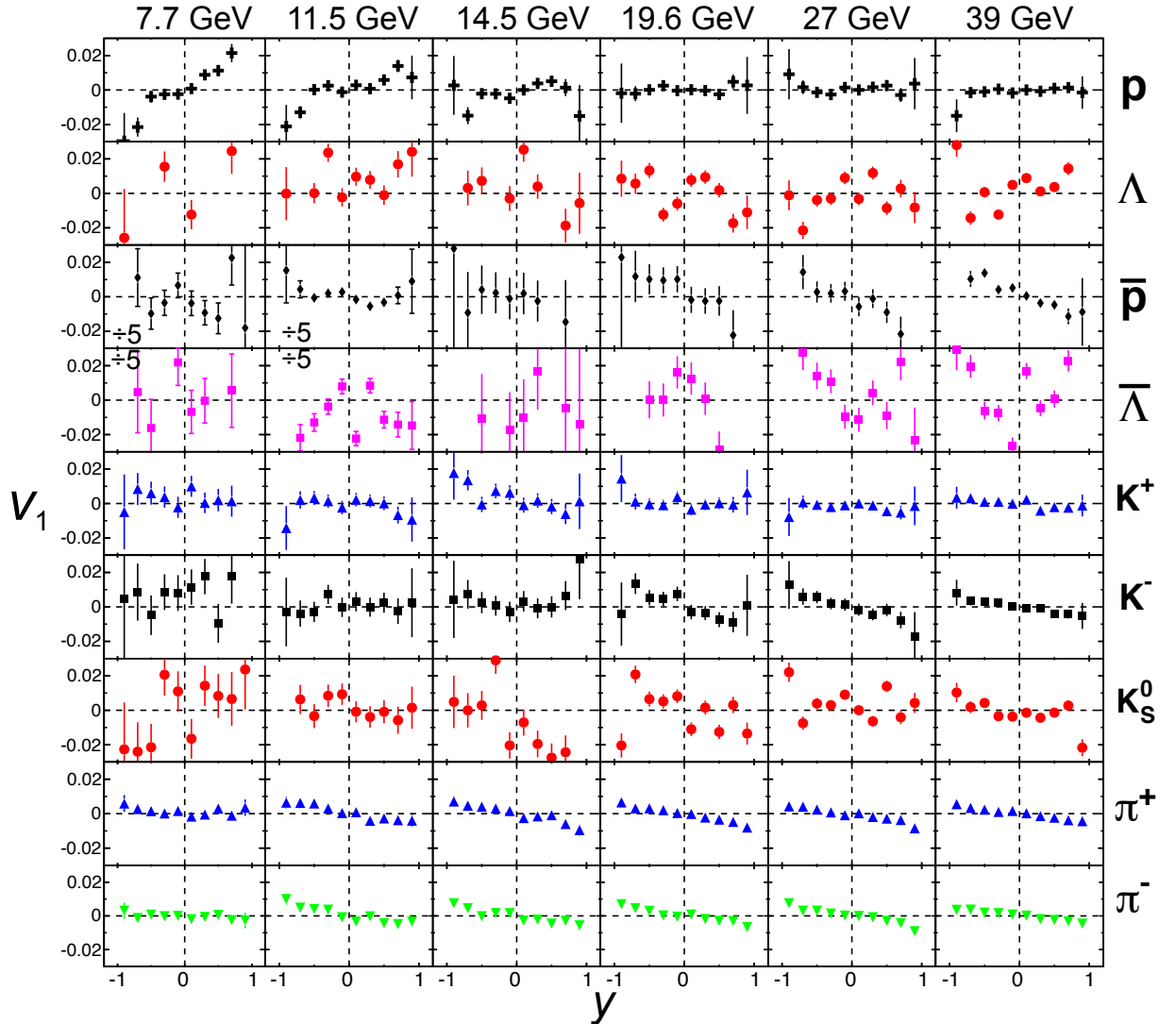


Figure 2.19: Directed flow (v_1) as a function of rapidity for p , Λ , \bar{p} , $\bar{\Lambda}$, K^\pm , K_s^0 and π^\pm in 0-10% centrality Au+Au collisions. Error bars are statistical. The v_1 magnitude is exceptionally large for \bar{p} and $\bar{\Lambda}$ at 7.7 and 11.5 GeV, and hence for only those panels, v_1 and its errors are divided by 5 to fit on the common vertical scale.

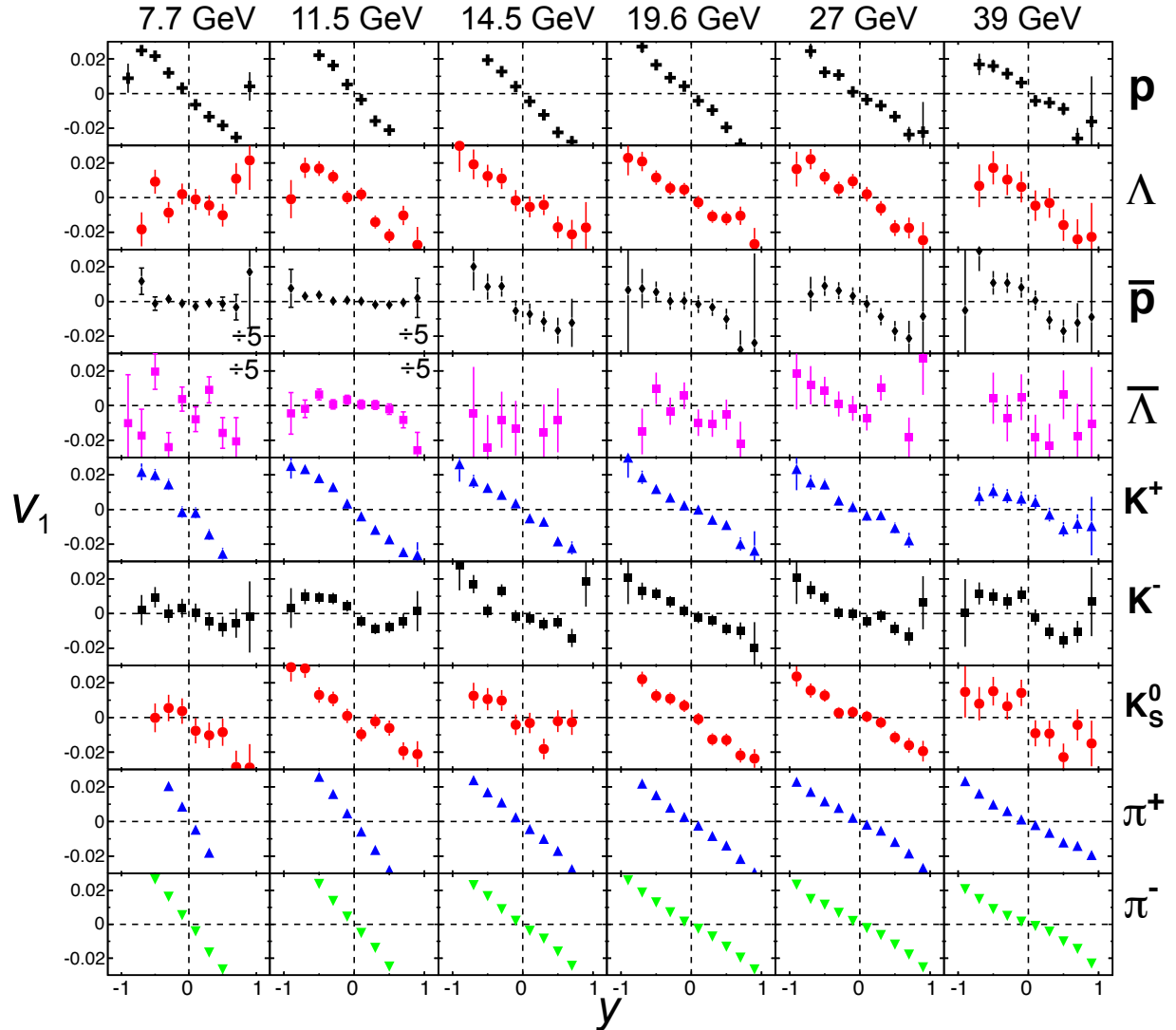


Figure 2.20: Directed flow (v_1) as a function of rapidity for p , Λ , \bar{p} , $\bar{\Lambda}$, K^\pm , K_s^0 and π^\pm in 40-80% centrality Au+Au collisions. Error bars are statistical. The v_1 magnitude is exceptionally large for \bar{p} and $\bar{\Lambda}$ at 7.7 and 11.5 GeV, and hence for only those panels, v_1 and its errors are divided by 5 to fit on the common vertical scale.

2.2.3 Different Definitions of Wide Centrality Bins

Centralities for Au+Au collisions are divided into nine bins as shown in Table 2.2. The intermediate centrality class that has already been studied in detail is a combination of three centrality bins: four, five and six. The effect of changing the upper and lower limit of the intermediate centrality class is investigated in Figure 2.21. It is seen that the qualitative trend of dv_1/dy doesn't depend on the exact definition of the intermediate centrality interval, but the depth and significance of the minimum for baryons (p and Λ) changes with different definitions.

Overall, Figure 2.21 allows the study of Ref. [49] to be revisited with a new energy point close to the position of the minimum in proton directed flow, and with a new baryon species, among other enhancements. The evidence for the phenomenon called “collapse of directed flow” is significantly strengthened.

Figure 2.21 contains hints that the BES-I dataset for 14.5 GeV does not always lie on the smooth trend defined by the other BES energies, but the departure is still within errors. There are similar hints in other BES analysis, and one possible explanation is the added material of the Heavy Flavor Tracker close to the primary vertex. Further study of this issue is continuing.

When more statistics will available from BES-II running in 2019 and 2020 [16], then a clearer conclusion on all the physics topics considered in this dissertation will likely be reached.

Centrality Bin	Centrality Percentage	Default	Trail-1
0	70-80	Peripheral	Peripheral
1	60-70		Intermediate
2	50-60		Centrality
3	40-50		Central
4	30-40		Central
5	20-30		Central
6	10-20		Central
7	5-10		Central
8	0-5		Central

Table 2.2: Alternative groupings of coarse centrality bins.

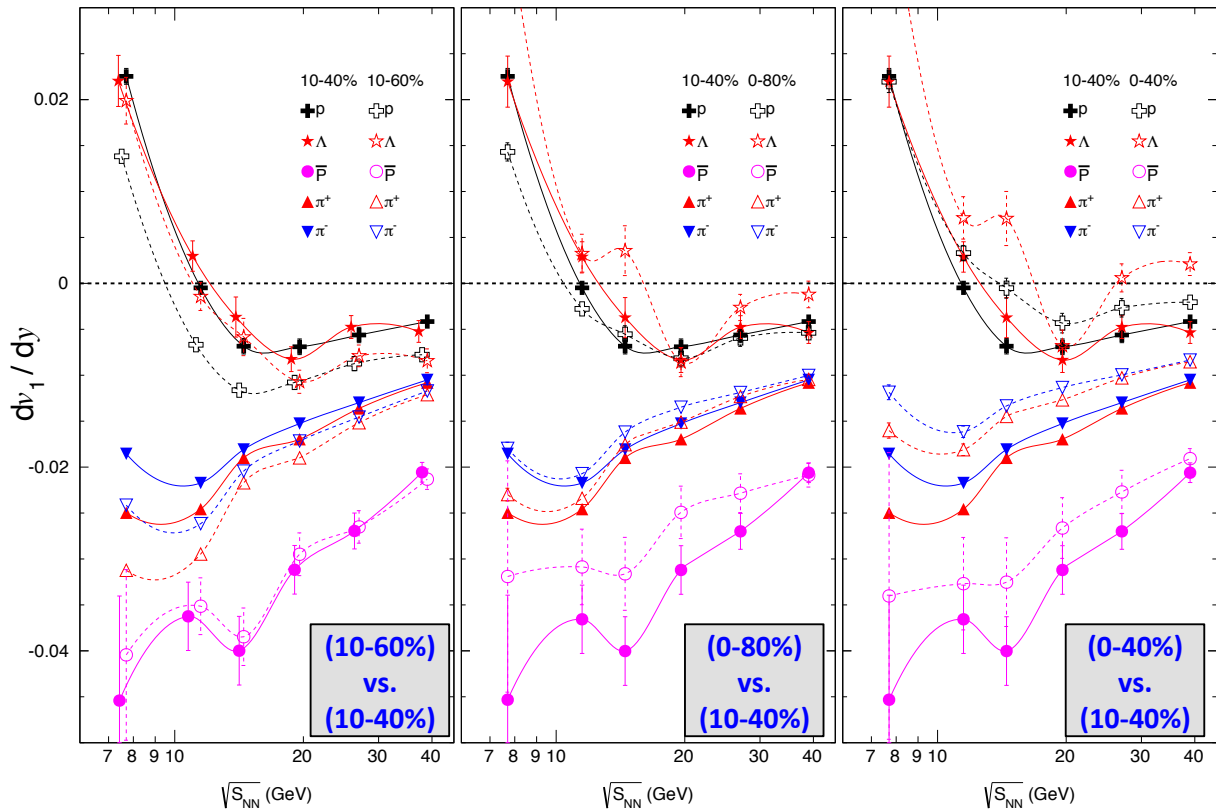


Figure 2.21: Comparison of dv_1/dy for different combinations of centrality bins with the default intermediate-centrality class. Error bars are statistical.

2.3 Centrality Dependence of Directed Flow

The strong centrality dependence of the event plane resolution requires us to calculate directed flow in narrow centrality bins, and then correct for the event plane resolution. During these steps, I have observed that dv_1/dy for the various particle species depends not only on the beam energy, but also on centrality for a given beam energy. The top panels of Figures 2.22, 2.23, 2.24, 2.25 show the centrality dependence of dv_1/dy for particles p , Λ , π^+ and π^- respectively. Results for \bar{p} and $\bar{\Lambda}$ are not discussed due to limited statistics. Protons, charged pions and Λ s shows strong centrality dependence at all beam energies. Furthermore, protons and Λ s show a sign change in dv_1/dy as a function of centrality at lower beam energies. However, these results are hampered by marginal statistics, especially for the most central and most peripheral collisions. The top panels of Figures 2.26, 2.27, 2.28 show the centrality dependence of dv_1/dy for K^+ , K^- and K_S^0 , respectively. Notice that the measured dv_1/dy for K^+ shows a moderately strong centrality dependence, whereas K^- and K_S^0 tends to show a more flat distribution. With the possible exception of charged pions, the centrality dependence of dv_1/dy is hampered by poor statistics. With the greatly improved statistics of BES-II running in 2019 and 2020, we can expect more promising results. The bottom panels of the above figures show UrQMD, where p shows strong centrality dependence for almost all the energies, while centrality dependence for Λ is much weaker in UrQMD calculations. Charged pions, charged kaons and K_S^0 from UrQMD show very weak centrality dependence at most of the studied beam energies.

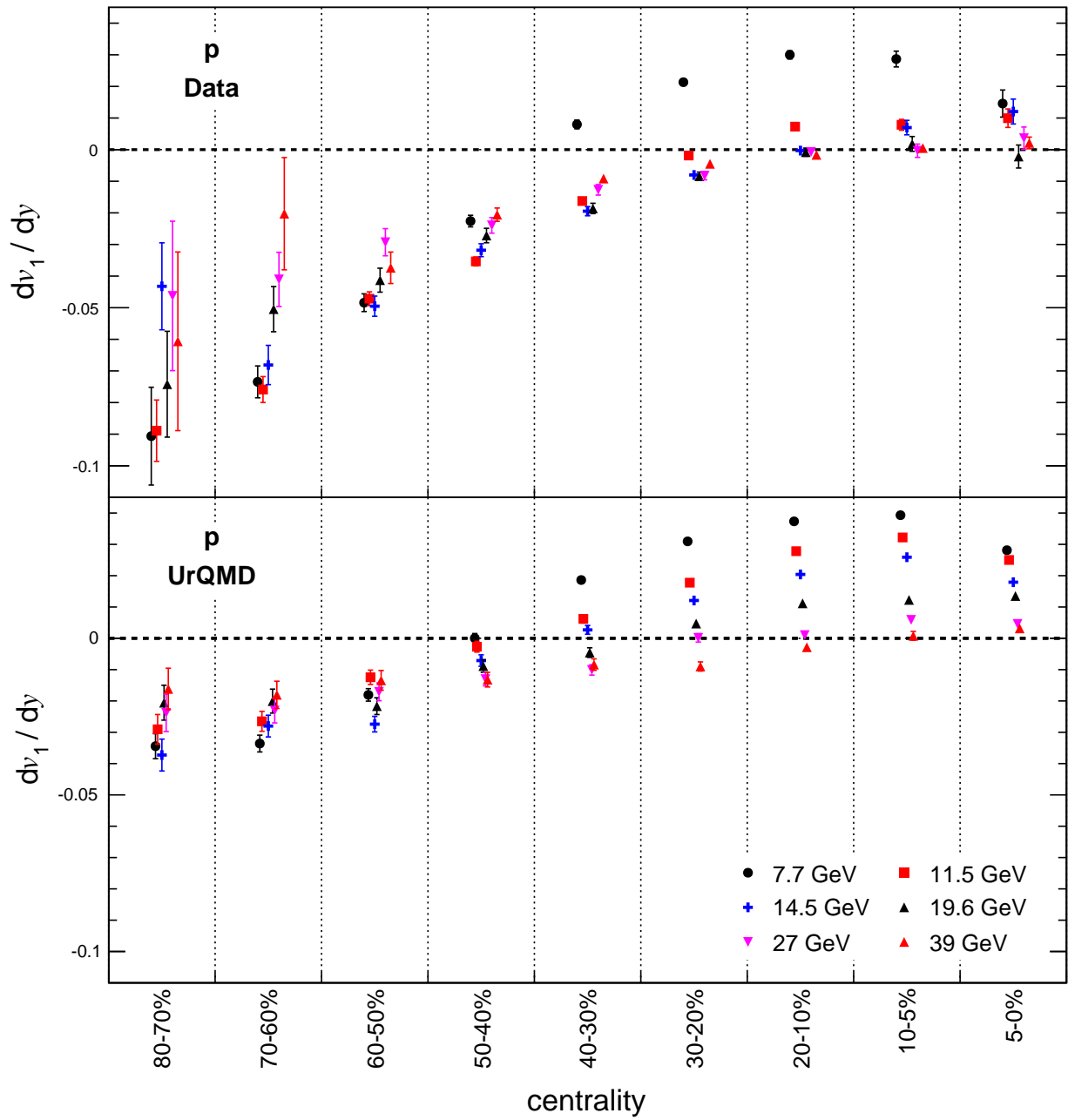


Figure 2.22: dv_1/dy near midrapidity as a function of centrality for p . Top panel from STAR data and bottom panel is from UrQMD. Error bars are statistical. In general, systematic errors are comparable to statistical errors, but are omitted to reduce clutter.

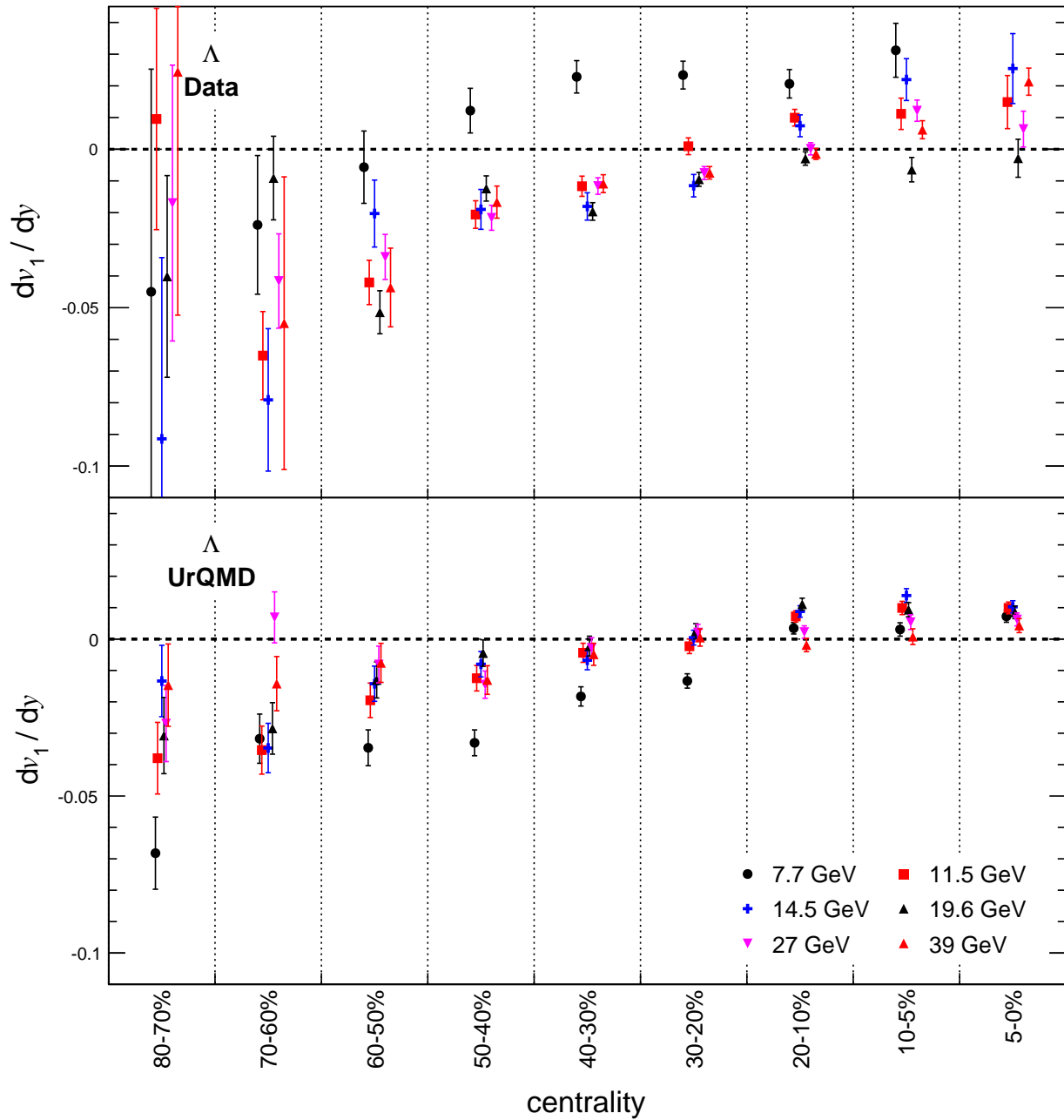


Figure 2.23: dv_1/dy near midrapidity as a function of centrality for Λ . Top panel from STAR data and bottom panel is from UrQMD. Error bars are statistical. In general, systematic errors are comparable to statistical errors, but are omitted to reduce clutter.

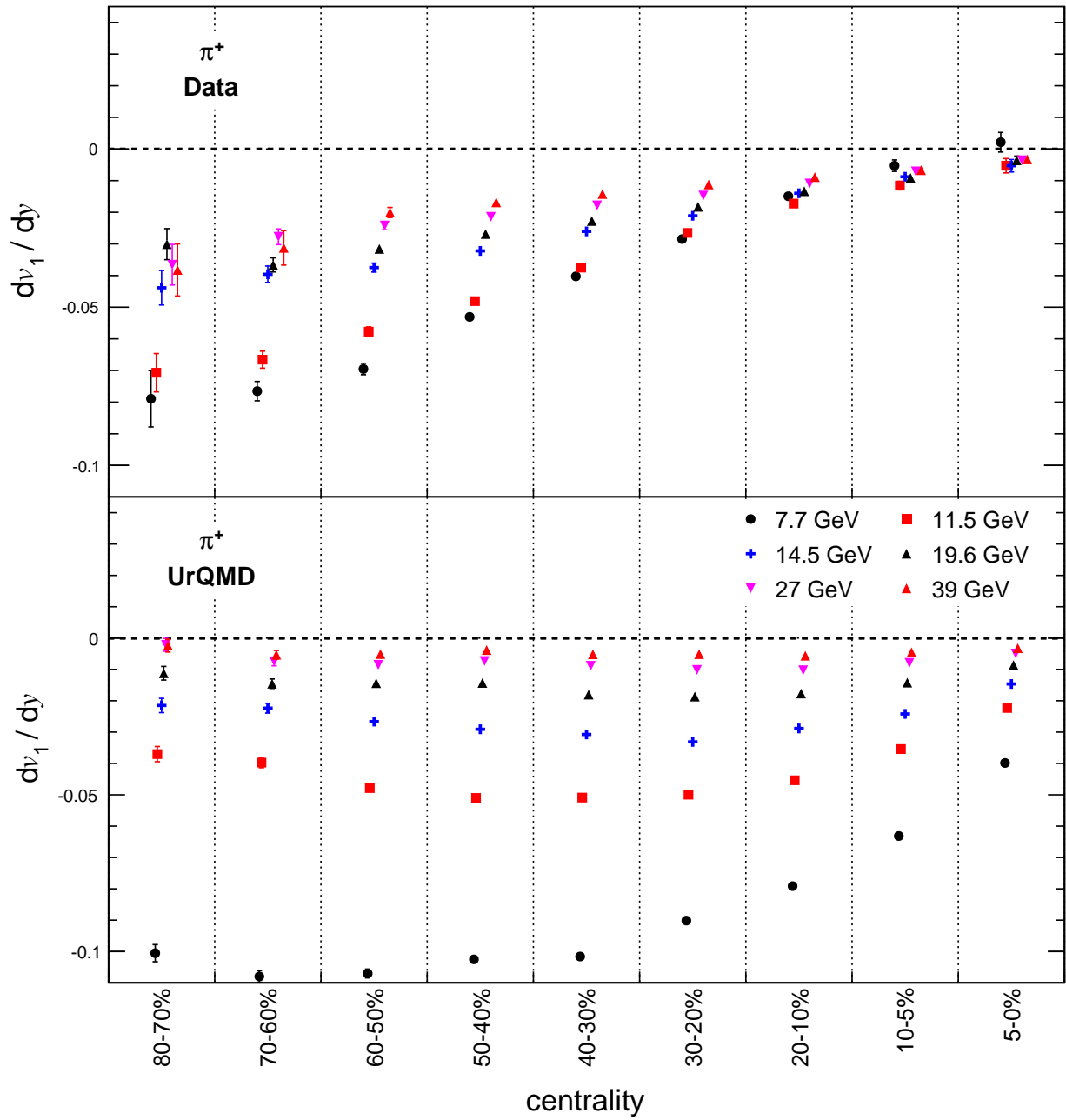


Figure 2.24: dv_1/dy near midrapidity as a function of centrality for π^+ . Top panel from STAR data and bottom panel is from UrQMD. Error bars are statistical. In general, systematic errors are comparable to statistical errors, but are omitted to reduce clutter.

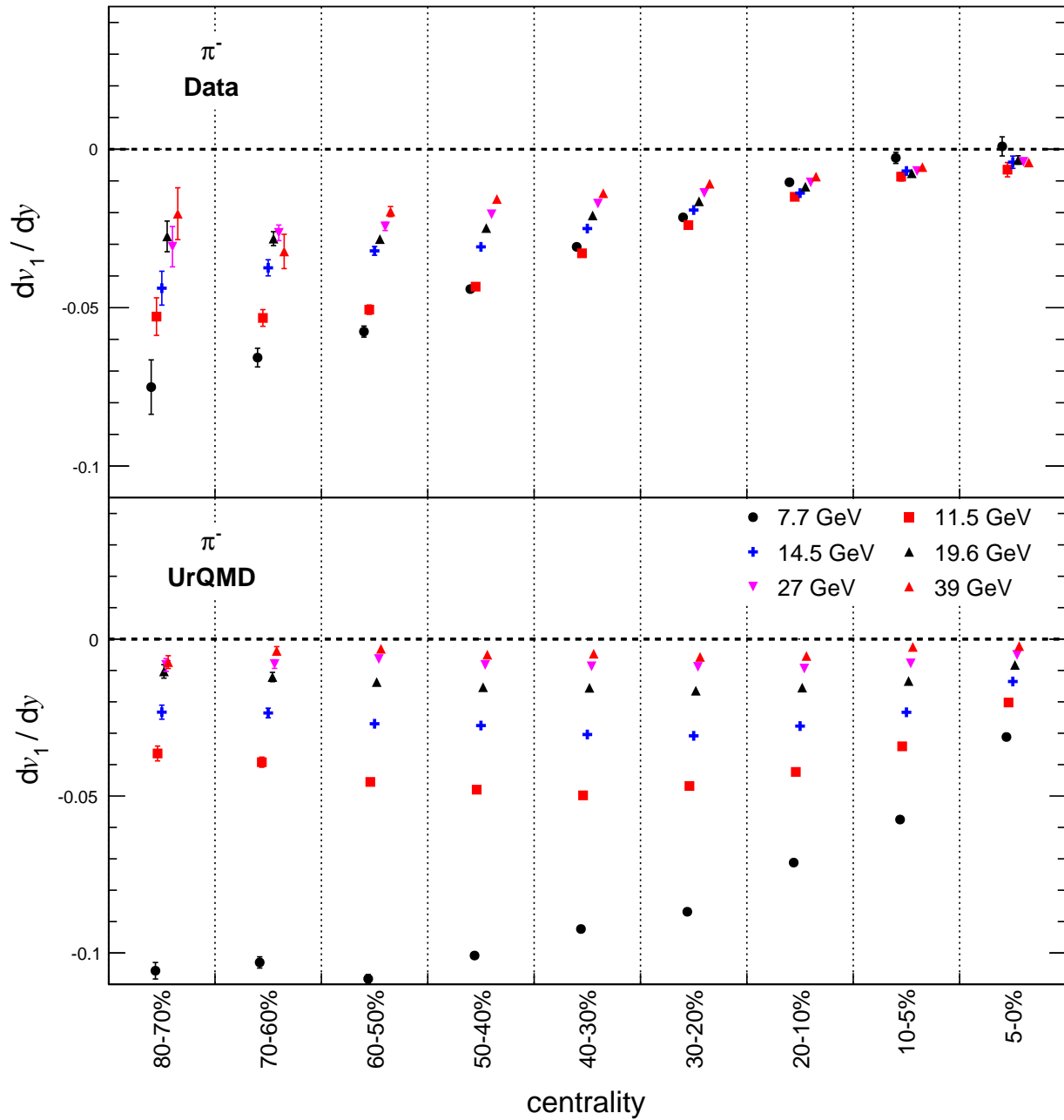


Figure 2.25: dv_1/dy near midrapidity as a function of centrality for π^- . Top panel from STAR data and bottom panel is from UrQMD. Error bars are statistical. In general, systematic errors are comparable to statistical errors, but are omitted to reduce clutter.

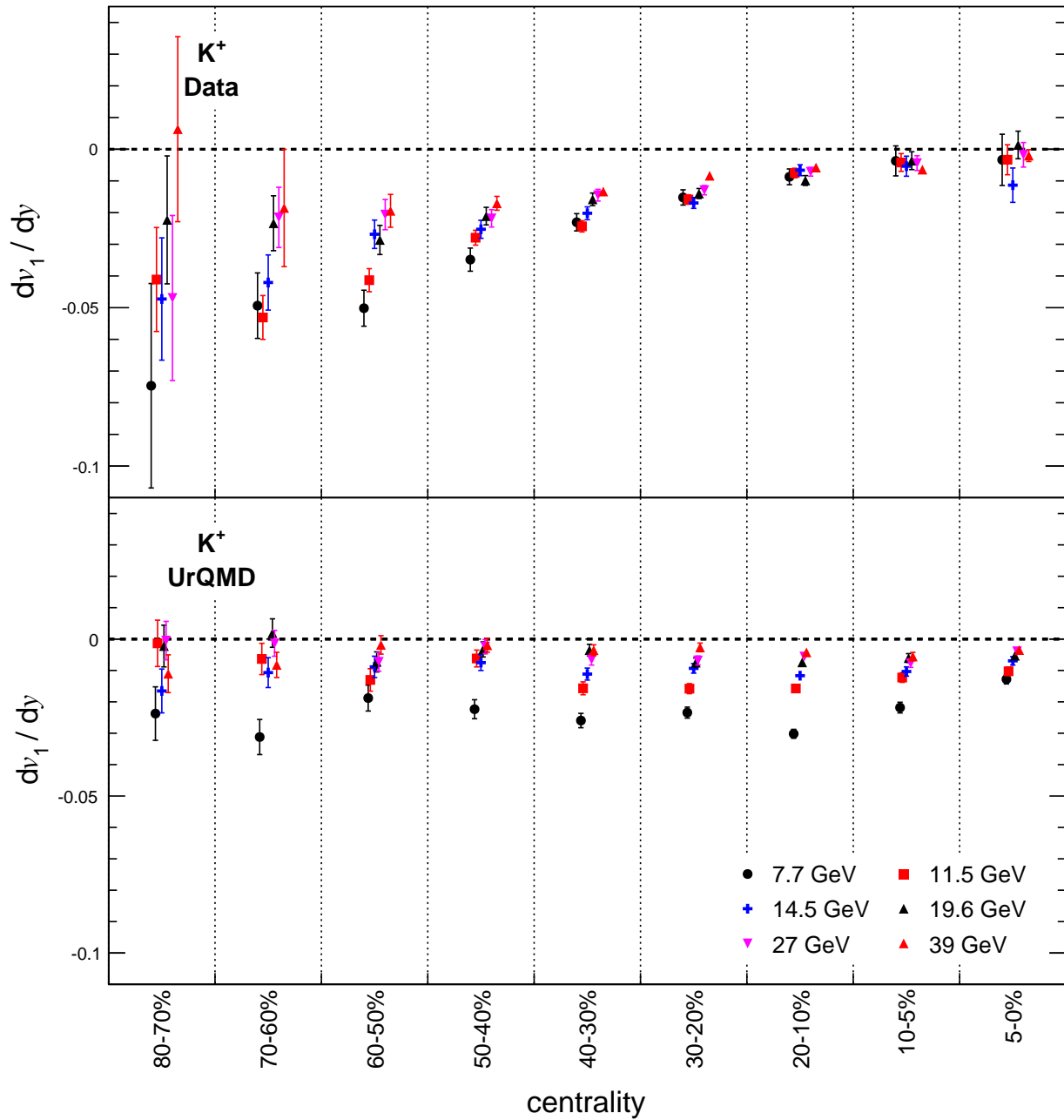


Figure 2.26: dv_1/dy near midrapidity as a function of centrality for K^+ . Top panel from STAR data and bottom panel is from UrQMD. Error bars are statistical. In general, systematic errors are comparable to statistical errors, but are omitted to reduce clutter.

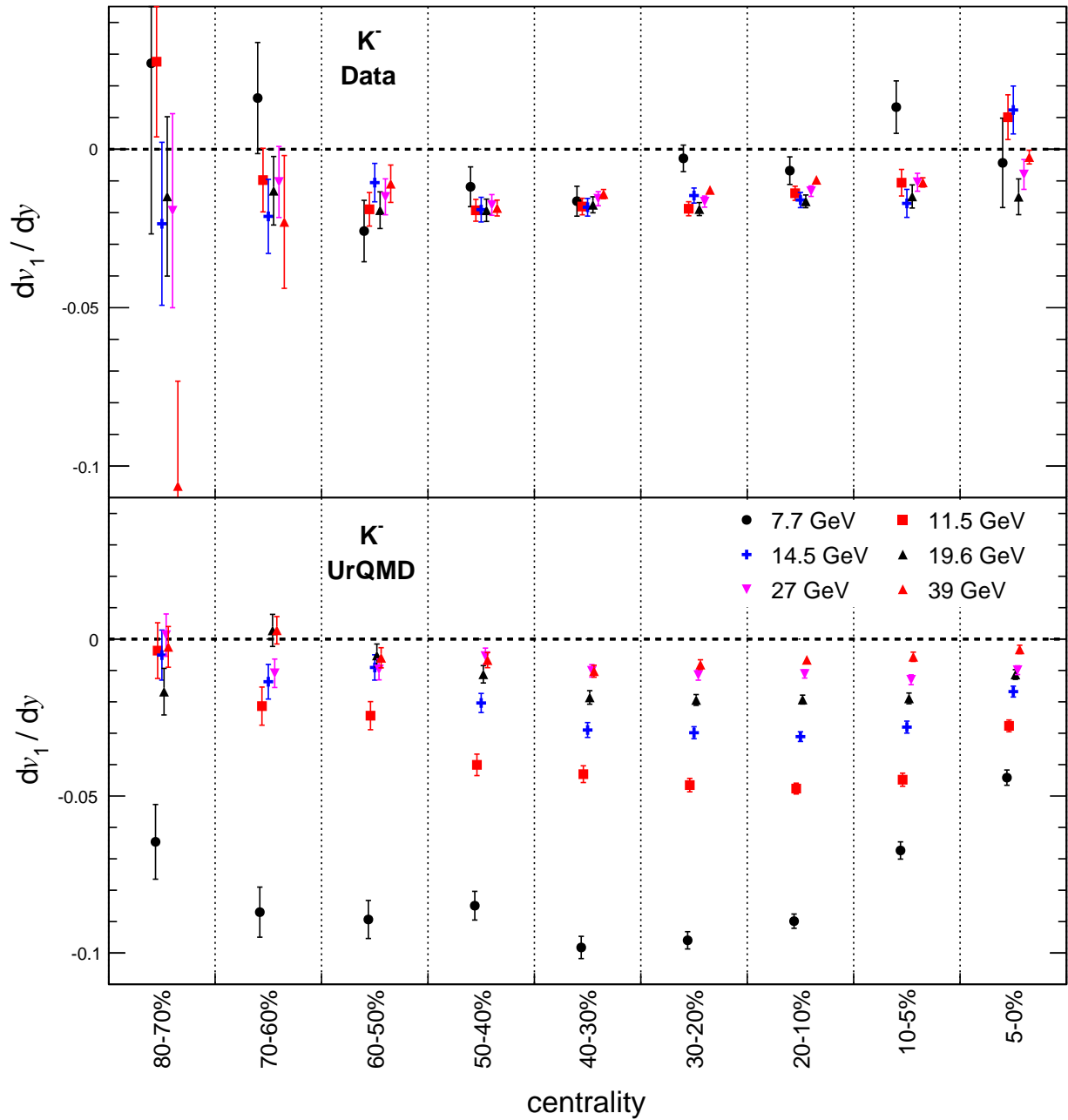


Figure 2.27: dv_1/dy near midrapidity as a function of centrality for K^- . Top panel from STAR data and bottom panel is from UrQMD. Error bars are statistical. In general, systematic errors are comparable to statistical errors, but are omitted to reduce clutter.

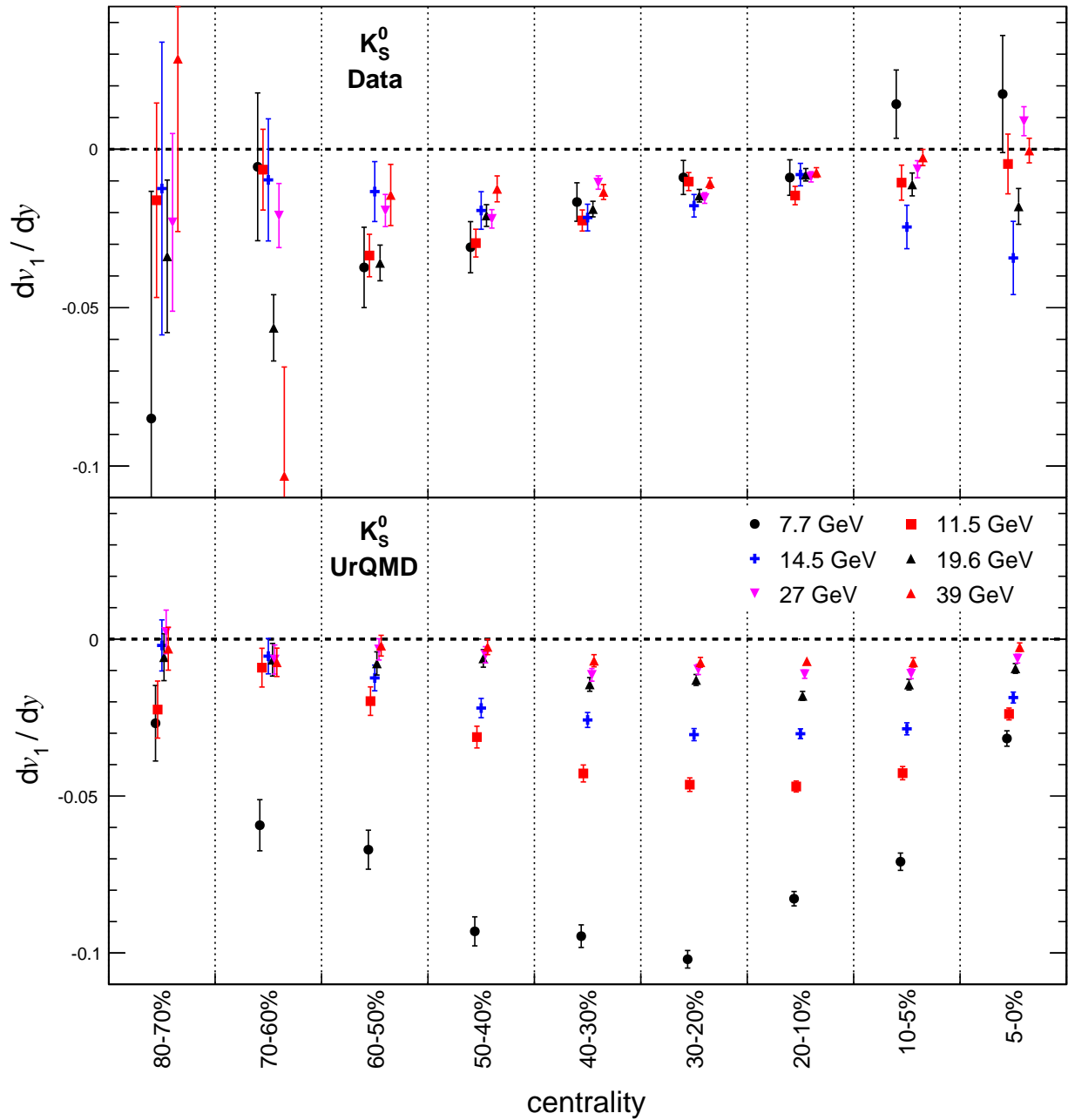


Figure 2.28: dv_1/dy near midrapidity as a function of centrality for K_S^0 . Top panel from STAR data and bottom panel is from UrQMD. Error bars are statistical. In general, systematic errors are comparable to statistical errors, but are omitted to reduce clutter.

The systematic error calculation for centrality dependence of dv_1/dy is very similar to the beam-energy dependence as explained in Section 1.4.3. Parameters and cuts are varied for the detector acceptance and the efficiencies. The systematic error in centrality for dv_1/dy is shown in Figures 2.29, 2.30 for p , Λ , π^+ and π^- at representative beam energies of 11.5 and 39 GeV respectively. Similarly, Figures 2.29 and 2.30 show the same for K^\pm and K_S^0 at representative beam energies of 11.5 and 39 GeV, respectively. Point-by-point systematic errors are comparable to statistical errors for all particle species at all beam energies.

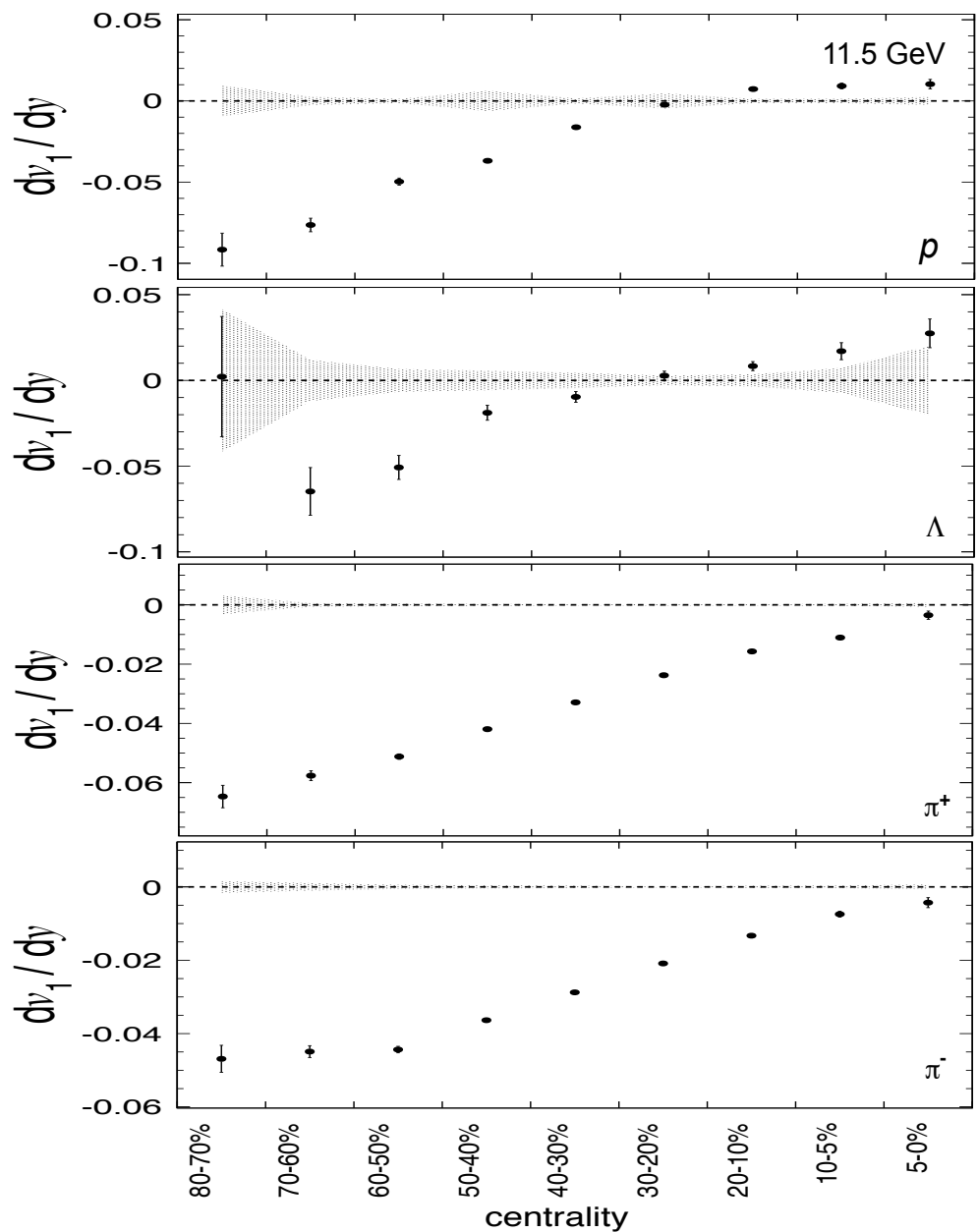


Figure 2.29: Systematic error for dv_1/dy as a function of centrality is shown for p , Λ , π^+ and π^- at a beam energy of 11.5 GeV.

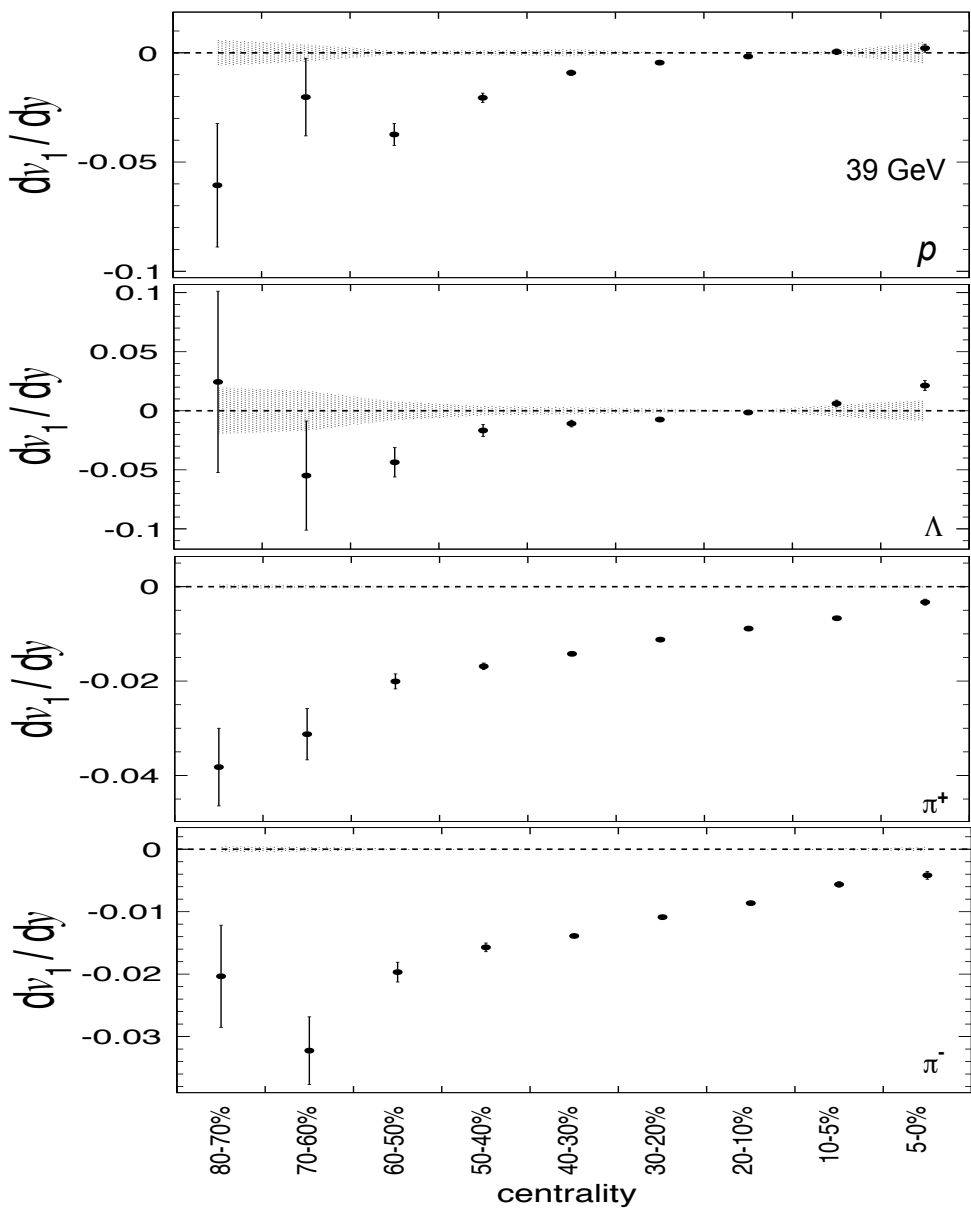


Figure 2.30: Systematic error for $d\nu_1/dy$ as a function of centrality is shown for p , Λ , π^+ and π^- at a beam energy of 39 GeV.

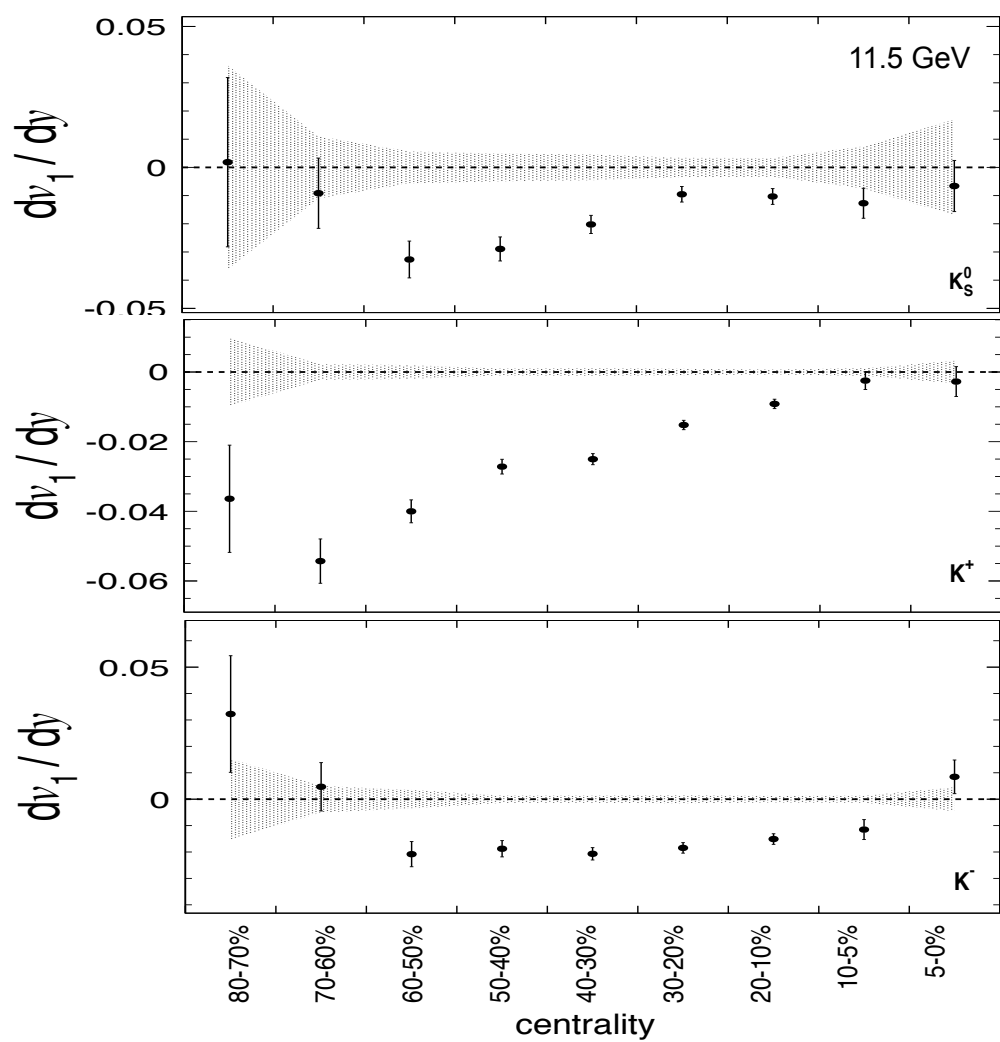


Figure 2.31: Systematic error for dv_1/dy as a function of centrality is shown for K^\pm and K_S^0 at a beam energy of 39 GeV.

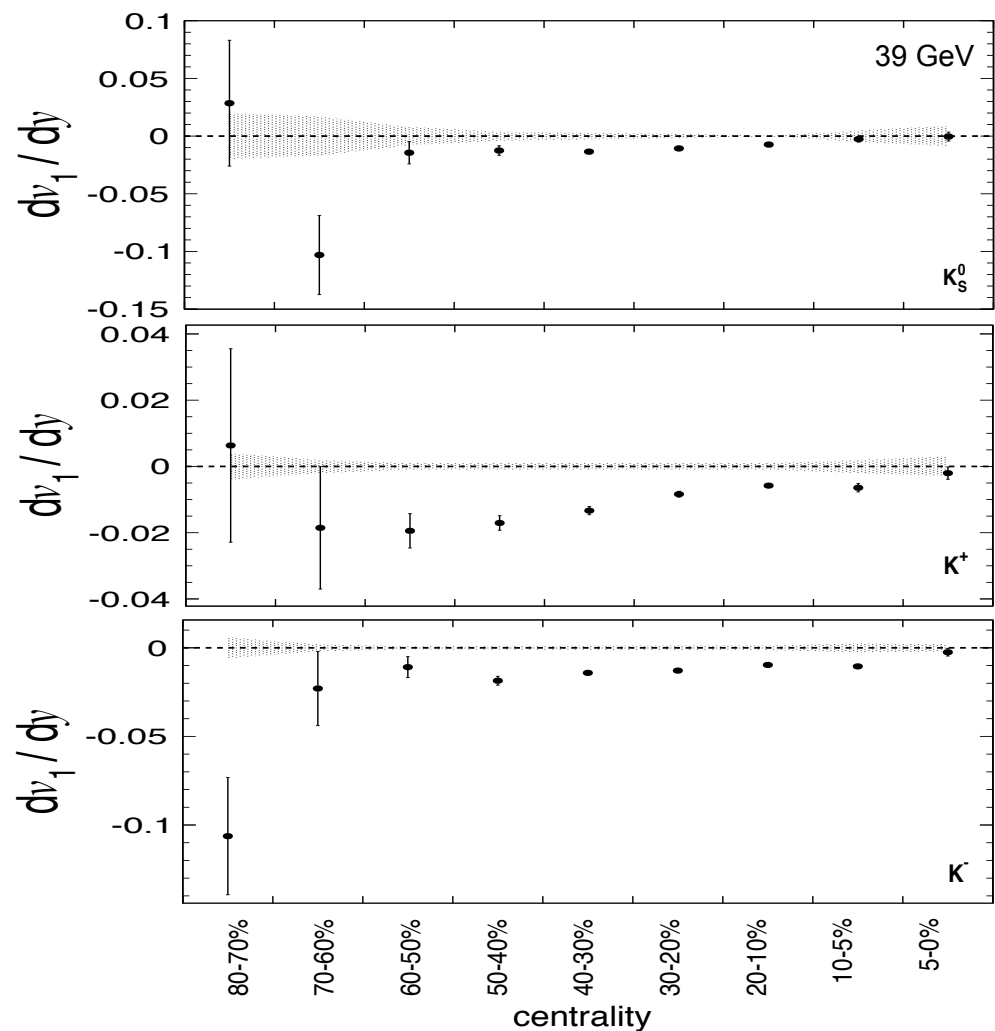


Figure 2.32: Systematic error for dv_1/dy as a function of centrality is shown for K^\pm and K_S^0 at a beam energy of 39 GeV.

Bibliography

- [1] K. G. Wilson, Phys. Rev. D **10**, 2445–2459 (1974).
- [2] F. Karsch, Nucl. Phys. **A698**, 199–208 (2002), arXiv:hep-ph/0103314 [hep-ph].
- [3] Y. Aoki, Z. Fodor, S. D. Katz, *et al.*, Phys. Lett. **B643**, 46–54 (2006), arXiv:hep-lat/0609068 [hep-lat].
- [4] Y. Aoki, S. Borsanyi, S. Durr, *et al.*, JHEP **06**, 088 (2009), arXiv:0903.4155 [hep-lat].
- [5] S. Borsanyi, Z. Fodor, C. Hoelbling, *et al.*, JHEP **09**, 073 (2010), arXiv:1005.3508 [hep-lat].
- [6] A. Bazavov *et al.*, Phys. Rev. **D85**, 054503 (2012), arXiv:1111.1710 [hep-lat].
- [7] Y. Aoki, G. Endrodi, Z. Fodor, *et al.*, Nature **443**, 675–678 (2006), arXiv:hep-lat/0611014 [hep-lat].
- [8] S. Ejiri, Phys. Rev. **D78**, 074507 (2008), arXiv:0804.3227 [hep-lat].
- [9] E. S. Bowman and J. I. Kapusta, Phys. Rev. **C79**, 015202 (2009), arXiv:0810.0042 [nucl-th].
- [10] E. Laermann and O. Philipsen, Ann. Rev. Nucl. Part. Sci. **53**, 163–198 (2003), arXiv:hep-ph/0303042 [hep-ph].
- [11] J. Stachel and K. Reygers, *Space-time evolution of the QGP*, (2015) http://www.physi.uni-heidelberg.de/~reygers/lectures/2015/qgp/qgp2015_06_space_time_evo.pdf.

- [12] *The star collaboration*, <http://www.star.bnl.gov/>.
- [13] *The phenix collaboration*, <http://www.phenix.bnl.gov/>.
- [14] A. Aduszkiewicz, Acta Phys. Polon. **B43**, 635 (2012), arXiv:1201.5879 [nucl-ex].
- [15] *Alternating gradient synchrotron*, <https://www.bnl.gov/rhic/AGS.asp>.
- [16] L. Adamczyk *et al.*, STAR Note SN0598 (2014).
- [17] J. Cleymans, H. Oeschler, K. Redlich, *et al.*, Phys. Rev. **C73**, 034905 (2006), arXiv:hep-ph/0511094 [hep-ph].
- [18] L. Kumar, Nucl. Phys. **A931**, 1114–1119 (2014), arXiv:1408.4209 [nucl-ex].
- [19] S. Das, Nucl. Phys. **A904-905**, 891c–894c (2013), arXiv:1210.6099 [nucl-ex].
- [20] I. Arsene *et al.*, Nucl. Phys. **A757**, 1–27 (2005), arXiv:nucl-ex/0410020 [nucl-ex].
- [21] B. B. Back *et al.*, Nucl. Phys. **A757**, 28–101 (2005), arXiv:nucl-ex/0410022 [nucl-ex].
- [22] J. Adams *et al.*, Nucl. Phys. **A757**, 102–183 (2005), arXiv:nucl-ex/0501009 [nucl-ex].
- [23] K. Adcox *et al.*, Nucl. Phys. **A757**, 184–283 (2005), arXiv:nucl-ex/0410003 [nucl-ex].
- [24] B. Back *et al.*, *et al.*, *Hot & Dense QCD Matter*, White Paper submitted to the 2012 Nuclear Science Advisory Committee.
- [25] J. Adams *et al.*, Phys. Rev. Lett. **92**, 052302 (2004), arXiv:nucl-ex/0306007 [nucl-ex].
- [26] S. S. Adler *et al.*, Phys. Rev. Lett. **91**, 182301 (2003), arXiv:nucl-ex / 0305013 [nucl-ex].
- [27] L. Adamczyk *et al.*, Phys. Rev. **C88**, 014902 (2013), arXiv:1301.2348 [nucl-ex].
- [28] J. C. Dunlop, M. A. Lisa, and P. Sorensen, Phys. Rev. **C84**, 044914 (2011), arXiv:1107.3078 [hep-ph].
- [29] X.-N. Wang and M. Gyulassy, Phys. Rev. Lett. **68**, 1480–1483 (1992).

- [30] B. Berdnikov and K. Rajagopal, Phys. Rev. **D61**, 105017 (2000), arXiv:hep-ph / 9912274 [hep-ph].
- [31] M. A. Stephanov, Phys. Rev. Lett. **102**, 032301 (2009), arXiv:0809.3450 [hep-ph].
- [32] M. Cheng *et al.*, Phys. Rev. **D79**, 074505 (2009), arXiv:0811.1006 [hep-lat].
- [33] R. V. Gavai and S. Gupta, Phys. Lett. **B696**, 459–463 (2011), arXiv:1001.3796 [hep-lat].
- [34] Y. Hatta and M. A. Stephanov, Phys. Rev. Lett. **91**, 129901 (2003).
- [35] L. Adamczyk *et al.*, Phys. Rev. Lett. **112**, 032302 (2014), arXiv:1309.5681 [nucl-ex].
- [36] B.-J. Schaefer and J. Wambach, Phys. Rev. **D75**, 085015 (2007), arXiv:hep-ph / 0603256 [hep-ph].
- [37] A. M. Poskanzer and S. A. Voloshin, Phys. Rev. **C58**, 1671–1678 (1998), arXiv:nucl-ex/9805001 [nucl-ex].
- [38] H. Sorge, Phys. Rev. Lett. **78**, 2309–2312 (1997), arXiv:nucl-th/9610026 [nucl-th].
- [39] N. Herrmann, J. P. Wessels, and T. Wienold, Ann. Rev. Nucl. Part. Sci. **49**, 581–632 (1999).
- [40] B. Alver and G. Roland, Phys. Rev. **C81**, [Erratum: Phys. Rev.C82,039903(2010)], 054905 (2010), arXiv:1003.0194 [nucl-th].
- [41] C. M. Hung and E. V. Shuryak, Phys. Rev. Lett. **75**, 4003–4006 (1995), arXiv:hep-ph/9412360 [hep-ph].
- [42] D. H. Rischke, Y. Pursun, J. A. Maruhn, *et al.*, Heavy Ion Phys. **1**, 309–322 (1995), arXiv:nucl-th/9505014 [nucl-th].
- [43] H. Stocker, Nucl. Phys. **A750**, 121–147 (2005), arXiv:nucl-th/0406018 [nucl-th].

- [44] Yu. B. Ivanov, E. G. Nikonov, W. Noerenberg, *et al.*, Heavy Ion Phys. **15**, 117–130 (2002), arXiv:nucl-th/0011004 [nucl-th].
- [45] V. D. Toneev, E. G. Nikonov, B. Friman, *et al.*, Eur. Phys. J. **C32**, 399–415 (2003), arXiv:hep-ph/0308088 [hep-ph].
- [46] J. Brachmann, S. Soff, A. Dumitru, *et al.*, Phys. Rev. C **61**, 024909 (2000).
- [47] L. Csernai and D. Röhricht, Physics Letters B **458**, 454 –459 (1999).
- [48] R. J. M. Snellings, H. Sorge, S. A. Voloshin, *et al.*, Phys. Rev. Lett. **84**, 2803–2805 (2000), arXiv:nucl-ex/9908001 [nucl-ex].
- [49] L. Adamczyk *et al.*, Phys. Rev. Lett. **112**, 162301 (2014), arXiv:1401.3043 [nucl-ex].
- [50] R. C. P. Huovinen in Quark-Gluon Plasma 3 Eds: Hwa and X. N. Wang, World Scientific, Singapore, 616 (2003).
- [51] M. Bleicher and H. Stoecker, Phys. Lett. **B526**, 309–314 (2002), arXiv:hep-ph/0006147 [hep-ph].
- [52] Y. Guo, F. Liu, and A. Tang, Phys. Rev. C **86**, 044901 (2012).
- [53] C. Alt *et al.*, Phys. Rev. **C68**, 034903 (2003), arXiv:nucl-ex/0303001 [nucl-ex].
- [54] M. Isse, A. Ohnishi, N. Otuka, *et al.*, Phys. Rev. C **72**, 064908 (2005).
- [55] H. Liu *et al.*, Phys. Rev. Lett. **84**, 5488–5492 (2000), arXiv:nucl-ex/0005005 [nucl-ex].
- [56] M. D. Partlan, S. Albergo, F. Bieser, *et al.*, Phys. Rev. Lett. **75**, 2100–2103 (1995).
- [57] J. Barrette, R. Bellwied, S. Bennett, *et al.*, Phys. Rev. C **56**, 3254–3264 (1997).
- [58] S. A. Moszkowski, Phys. Rev. D **9**, 1613–1625 (1974).
- [59] P. Chung *et al.*, Phys. Rev. Lett. **86**, 2533–2536 (2001), arXiv:nucl-ex / 0101002 [nucl-ex].

- [60] S. A. Bass *et al.*, Prog. Part. Nucl. Phys. **41**, [Prog. Part. Nucl. Phys.41,225(1998)], 255–369 (1998), arXiv:nucl-th/9803035 [nucl-th].
- [61] M. Bleicher *et al.*, J. Phys. **G25**, 1859–1896 (1999), arXiv:hep-ph/9909407 [hep-ph].
- [62] A. Muronga, Phys. Rev. C **69**, 034903 (2004).
- [63] J. Steinheimer, J. Auvinen, H. Petersen, *et al.*, Phys. Rev. C **89**, 054913 (2014).
- [64] V. P. Konchakovski, W. Cassing, Yu. B. Ivanov, *et al.*, Phys. Rev. C **90**, 014903 (2014), arXiv:1404.2765 [nucl-th].
- [65] Y. Nara, N. Otuka, A. Ohnishi, *et al.*, Phys. Rev. C **61**, 024901 (1999).
- [66] D. E. Kahana, D. Keane, Y. Pang, *et al.*, Phys. Rev. Lett. **74**, 4404–4407 (1995), arXiv:nucl-th/9405017 [nucl-th].
- [67] B.-A. Li and C. M. Ko, Phys. Rev. C **58**, 1382–1384 (1998), arXiv:nucl-th/9807088 [nucl-th].
- [68] Y. Nara, A. Ohnishi, and H. Stoecker, (2016), arXiv:1601.07692 [hep-ph].
- [69] T. Ludlam, Nuclear Instruments and Methods in Physics Research Section A: Accelerators, Spectrometers, Detectors and Associated Equipment **499**, The Relativistic Heavy Ion Collider Project: RHIC and its Detectors, 428 –432 (2003).
- [70] M Adamczyk, L Antvorskov, K Ashktorab, *et al.*, Nuclear Instruments and Methods in Physics Research Section A: Accelerators, Spectrometers, Detectors and Associated Equipment **499**, The Relativistic Heavy Ion Collider Project: RHIC and its Detectors, 437 –468 (2003).
- [71] B. Back *et al.*, Nuclear Instruments and Methods in Physics Research Section A: Accelerators, Spectrometers, Detectors and Associated Equipment **499**, The Relativistic Heavy Ion Collider Project: RHIC and its Detectors, 603 –623 (2003).

- [72] K. Adcox *et al.*, Nuclear Instruments and Methods in Physics Research Section A: Accelerators, Spectrometers, Detectors and Associated Equipment **499**, The Relativistic Heavy Ion Collider Project: RHIC and its Detectors, 469 –479 (2003).
- [73] K. Ackermann *et al.*, Nuclear Instruments and Methods in Physics Research Section A: Accelerators, Spectrometers, Detectors and Associated Equipment **499**, The Relativistic Heavy Ion Collider Project: RHIC and its Detectors, 624 –632 (2003).
- [74] *RHIC accelerator complex*, (2016) <https://www.bnl.gov/rhic/complex.asp>.
- [75] M. Anderson, J. Berkovitz, W. Betts, *et al.*, Nuclear Instruments and Methods in Physics Research Section A: Accelerators, Spectrometers, Detectors and Associated Equipment **499**, The Relativistic Heavy Ion Collider Project: RHIC and its Detectors, 659 –678 (2003).
- [76] L. Kotchenda, S. Kozlov, P. Kravtsov, *et al.*, Nuclear Instruments and Methods in Physics Research Section A: Accelerators, Spectrometers, Detectors and Associated Equipment **499**, The Relativistic Heavy Ion Collider Project: RHIC and its Detectors, 703 –712 (2003).
- [77] J. Abele, J. Berkovitz, J. Boehm, *et al.*, Nuclear Instruments and Methods in Physics Research Section A: Accelerators, Spectrometers, Detectors and Associated Equipment **499**, The Relativistic Heavy Ion Collider Project: RHIC and its Detectors, 692 –702 (2003).
- [78] F. Geurts, M. Shao, B. Bonner, *et al.*, Nuclear Instruments and Methods in Physics Research Section A: Accelerators, Spectrometers, Detectors and Associated Equipment **533**, Proceedings of the Seventh International Workshop on Resistive Plate Chambers and Related Detectors, 60 –64 (2004).

- [79] W. Llope, Nuclear Instruments and Methods in Physics Research Section A: Accelerators, Spectrometers, Detectors and Associated Equipment **661**, Supplement 1, X. Workshop on Resistive Plate Chambers and Related Detectors (RPC 2010), S110 –S113 (2012).
- [80] W. J. Llope *et al.*, Nucl. Instrum. Meth. **A522**, 252–273 (2004), arXiv:nucl-ex / 0308022 [nucl-ex].
- [81] Y. Pandit, Ph.d. Dissertation (Kent State University, Kent, OH, July 2012).
- [82] D. Kharzeev and M. Nardi, Phys. Lett. **B507**, 121–128 (2001), arXiv:nucl-th/0012025 [nucl-th].
- [83] E. Sangaline, Ph.d. Dissertation (University of California, Davis, CA, 2014).
- [84] H. Bichsel, Nucl. Instrum. Meth. **A562**, 154–197 (2006).
- [85] M. Shao, O. Yu. Barannikova, X. Dong, *et al.*, Nucl. Instrum. Meth. **A558**, 419–429 (2006), arXiv:nucl-ex/0505026 [nucl-ex].
- [86] C. Amsler *et al.*, Phys. Lett. **B667**, 1–1340 (2008).
- [87] J. Beringer *et al.*, Phys. Rev. **D86**, 010001 (2012).
- [88] H. Long, Ph.d. Dissertation (University of California, Los Angeles, CA, 2002).
- [89] M. Lisa and I. Upsal, private communication, Aug. 2014.
- [90] I. Selyuzhenkov and S. Voloshin, Phys. Rev. **C77**, 034904 (2008), arXiv:0707.4672 [nucl-th].
- [91] J. Barrette *et al.*, Phys. Rev. **C56**, 3254–3264 (1997), arXiv:nucl-ex/9707002 [nucl-ex].
- [92] J.-Y. Ollitrault, Nucl. Phys. **A638**, 195–206 (1998), arXiv:nucl-ex/9802005 [nucl-ex].
- [93] N. Borghini, P. M. Dinh, J.-Y. Ollitrault, *et al.*, Phys. Rev. **C66**, 014901 (2002), arXiv:nucl-th/0202013 [nucl-th].

- [94] G. Agakishiev *et al.*, Phys. Rev. **C85**, 014901 (2012), arXiv:1109.5446 [nucl-ex].
- [95] P. Danielewicz, Phys. Rev. **C51**, 716–750 (1995), arXiv:nucl-th/9408018 [nucl-th].
- [96] J. Barrette *et al.*, Phys. Rev. **C55**, [Erratum: Phys. Rev.C56,2336(1997)], 1420–1430 (1997), arXiv:nucl-ex/9610006 [nucl-ex].
- [97] B. I. Abelev *et al.*, Phys. Rev. **C75**, 054906 (2007), arXiv:nucl-ex/0701010 [nucl-ex].